

The Dynamic Range of Bursting in a Model Respiratory Pacemaker Network*

Janet Best[†], Alla Borisyuk[†], Jonathan Rubin[‡], David Terman[§], and Martin Wechselberger[†]

Abstract. A network of excitatory neurons within the pre-Bötzinger complex (pre-BötC) of the mammalian brain stem has been found experimentally to generate robust, synchronized population bursts of activity. An experimentally calibrated model for pre-BötC cells yields typical square-wave bursting behavior in the absence of coupling, over a certain parameter range, with quiescence or tonic spiking outside of this range. Previous simulations of this model showed that the introduction of synaptic coupling extends the bursting parameter range significantly and induces complex effects on burst characteristics. In this paper, we use geometric dynamical systems techniques, predominantly a fast/slow decomposition and bifurcation analysis approach, to explain these effects in a two-cell model network. Our analysis yields the novel finding that, over a broad range of synaptic coupling strengths, the network can support two qualitatively distinct forms of synchronized bursting, which we call symmetric and asymmetric bursting, as well as both symmetric and asymmetric tonic spiking. By elucidating the dynamical mechanisms underlying the transitions between these states, we also gain insight into how relevant parameters influence burst duration and interburst intervals. We find that, in the two-cell network with synaptic coupling, the stable family of periodic orbits for the fast subsystem features spike asynchrony within otherwise synchronized bursts and terminates in a saddle-node bifurcation, rather than in a homoclinic bifurcation, over a wide parameter range. As a result, square-wave bursting is replaced by what we call top hat bursting (also known as fold/fold cycle bursting), at least for a broad range of parameter values. Further, spike asynchrony is a key ingredient in shaping the dynamic range of bursting, leading to a significant enhancement in the parameter range over which bursting occurs and an abrupt increase in burst duration as an appropriate parameter is varied.

Key words. square-wave bursting, fast/slow decomposition, synaptic coupling, averaged equations, bifurcation analysis, respiratory pacemaker

AMS subject classifications. 34C15, 34C29, 37G15, 37N25, 92C20

DOI. 10.1137/050625540

1. Introduction. The inspiratory phase of the respiratory rhythm is believed to originate in a group of neurons in a region of the brain stem referred to as the pre-Bötzinger complex (pre-BötC) [28]. Within the pre-BötC, when coupling among cells is removed, there are silent cells, cells that spike continuously, and intrinsically bursting cells that generate groups of spikes separated by pauses [28, 12, 14]. Cells in all of these classes seem capable of reg-

*Received by the editors February 28, 2005; accepted for publication (in revised form) by M. Golubitsky July 29, 2005; published electronically November 18, 2005. This research was supported by the National Science Foundation, through awards DMS-0414023 to JR, DMS-0414057 to DT, and DMS-0112050 to the Mathematical Biosciences Institute.

<http://www.siam.org/journals/siads/4-4/62554.html>

[†]The Mathematical Biosciences Institute, The Ohio State University, Columbus, OH 43210 (jbest@mbi.ohio-state.edu, borisyuk@mbi.ohio-state.edu, wm@mbi.ohio-state.edu).

[‡]Department of Mathematics and Center for the Neural Basis of Cognition, University of Pittsburgh, Pittsburgh, PA 15260 (rubin@math.pitt.edu).

[§]Department of Mathematics, The Ohio State University, Columbus, OH 43210 (terman@math.ohio-state.edu).

ular oscillatory bursting, if provided with appropriate inputs experimentally, and thus these cells are sometimes called “pacemaker cells.” Experiments in brain slices have shown that a synaptically coupled network of pre-BötC pacemaker cells can display synchronous bursting oscillations [28, 18].

In two papers, Butera and collaborators presented experimentally constrained conductance-based models for individual pacemaker cells in the pre-BötC as well as for a network of these cells [1, 2]. In the network, both excitatory synaptic coupling between cells and a depolarizing input current from a tonically firing population were included, whereas the persistence of respiratory rhythms in pre-BötC under experimental blockage of synaptic inhibition justified its omission [14]. For the most part, each cell was coupled to all other cells, although similar results were found with less complete connectivities. Following Butera, Rinzal, and Smith, let the parameter g_{syn-e} denote the maximal conductance of an excitatory synaptic input from one cell to another, and let $g_{tonic-e}$ denote the conductance of the tonic depolarizing current, which is taken to be identical for all cells. A focal point of the Butera network study was the characterization of the *dynamic range* of bursting in the model network. The dynamic range here refers both to the range of $g_{tonic-e}$ over which the network displays bursting behavior, for a fixed g_{syn-e} , and to the corresponding range of burst frequencies produced.

Uncoupled model pre-BötC cells are square-wave bursters, over a range of $g_{tonic-e}$. In their simulations, Butera, Rinzal, and Smith found that introducing synaptic coupling among identical model cells, by increasing g_{syn-e} from zero to a nonzero level, increased the range of $g_{tonic-e}$ over which synchronized bursting oscillations occurred, relative to the bursting range for a single cell [2]. More precisely, the coupled network would burst synchronously for the same $g_{tonic-e}$ values that led to single cell bursting, as well as for an interval of $g_{tonic-e}$ that would cause continuous firing in a single cell. This effect was nonmonotonic, such that as g_{syn-e} was increased, the bursting range of $g_{tonic-e}$ would reach a maximum and then would begin to shrink back toward that observed for $g_{syn-e} = 0$. Butera, Rinzal, and Smith also used simulations to map out the changes in burst frequency and other burst characteristics with changes in g_{syn-e} and $g_{tonic-e}$. In particular, they found that while the bursting range of $g_{tonic-e}$ increased as g_{syn-e} increased from zero, network bursts with at least some nonzero g_{syn-e} values achieved a more limited range of burst frequencies than achieved with $g_{syn-e} = 0$.

The primary goal of this work is to provide a thorough mathematical analysis of the mechanisms underlying most of these findings. We employ a fast/slow decomposition [20, 22] to focus on how changes in g_{syn-e} and $g_{tonic-e}$ affect the bifurcation structure of the Butera pacemaker cell model. This approach allows us to elucidate the nature of the transitions from quiescence to bursting and from bursting to spiking in the network, as g_{syn-e} and $g_{tonic-e}$ are separately varied. We note that while both g_{syn-e} and $g_{tonic-e}$ are conductances for inward, excitatory currents, increasing these parameters may have very different effects on network dynamics. In particular, increasing g_{syn-e} may transform the network from spiking to bursting and then back to spiking; however, increasing $g_{tonic-e}$ can never transform the network from spiking to bursting. Importantly, our analysis raises the distinction that bursting and tonic spiking in a coupled pair of cells can be *symmetric*, in that the trajectories converge to, and oscillate regularly about, an axis of symmetry, or *asymmetric*, depending on features that we derive from the network dynamics. In addition to explaining how these different activity patterns arise, our results include an analysis of transitions between them. In the bursting

regime, this leads to an understanding of how synaptic coupling and excitatory inputs combine to influence the silent and active phase durations, and hence the period, of bursting.

Because the Butera, Rinzel, and Smith pacemaker cell model is a square-wave burster under appropriate parameter choices, the results presented here advance the current mathematical understanding of transitions between activity modes in general networks of cells capable of square-wave bursting [20, 30, 31, 11, 22]. The analysis also demonstrates how coupling cells that exhibit one type of behavior, namely, spiking, can lead to a different firing pattern, namely, bursting. Furthermore, our results, while mathematical in character, are relevant to the study of the biology of respiration in that they elucidate dynamical mechanisms that can lead to various activity patterns, which may be experimentally distinguishable in the pre-BötC, along with the implications of these mechanisms for quantitative aspects of network activity.

In section 2 of the paper, we introduce the full Butera model and the details of the fast/slow decomposition that we employ, including the key mathematical features that combine to govern both the network dynamics in the model and the influence of $g_{tonic-e}$, g_{syn-e} on network behavior. This analysis, in the case $g_{syn-e} = 0$, explains the transition from quiescence to bursting to tonic spiking in a single uncoupled cell. Next, in section 3, we start with a brief discussion of how the transition from quiescence to bursting seen without synaptic coupling carries over directly to coupled cells. Following this, we turn to the much more complex transition from bursting to spiking in the presence of synaptic coupling. We progress through several levels of analysis of the associated phenomena. First, we consider the special case of a single self-coupled cell. Second, we consider a pair of coupled cells under a strong synchrony assumption. Finally, we consider a pair of coupled cells with no restrictions imposed on their evolution. This progression demonstrates how each aspect of the dynamics of the freely evolving coupled cell pair contributes to the overall transition landscape. In particular, our analysis illustrates how the asynchrony of spikes during the active phases of bursts can extend the dynamic range of bursting in a synaptically coupled pair of cells. In section 4, we explain how variations in g_{syn-e} and $g_{tonic-e}$ lead to changes in burst duration and interburst intervals, based on the bifurcation structures elucidated in the earlier sections. Finally, certain aspects of the qualitatively different transition mechanisms that we find underlying the switch between bursting and tonic spiking in different parameter regimes lead to different experimental implications, which we describe as part of the discussion in section 5.

2. Model and basic fast/slow decomposition.

2.1. The Butera model. The results of Butera, Rinzel, and Smith show that single-cell bursting, matching experimentally observed properties of pre-BötC cells, can be initiated by the fast activation of a persistent sodium current, I_{NaP} , and terminated by the slow inactivation of this same current [1]. Thus, using the Hodgkin–Huxley formalism, the membrane potential dynamics of each pre-BötC cell within a coupled network can be modeled by the equation

$$(1) \quad v'_i = (-I_{NaP} - I_{Na} - I_K - I_L - I_{tonic-e} - I_{syn-e})/C,$$

where each term on the right-hand side denotes an ionic current through the cell membrane and the derivative is with respect to time t . Specifically, we have $I_{NaP} = \bar{g}_{NaP} m_{P,\infty}(v_i) h_i(v_i -$

E_{Na}), $I_{Na} = \bar{g}_{Na} m_\infty^3(v_i)(1 - n_i)(v_i - E_{Na})$, $I_K = \bar{g}_K n_i^4(v_i - E_K)$, $I_L = \bar{g}_L(v_i - E_L)$, and $I_{tonic-e} = g_{tonic-e}(v_i - E_{syn-e})$. The functions and parameters in these currents are identical to those presented in [1] and are listed in the appendix for completeness. Units for all variables are also given in the appendix. These units are used for all simulations, figures, and analysis in this work, and we omit explicit mention of them throughout the rest of the paper. The dynamic auxiliary variables h_i, n_i satisfy

$$(2) \quad h'_i = \epsilon(h_\infty(v_i) - h_i)/\tau_h(v_i),$$

$$(3) \quad n'_i = (n_\infty(v_i) - n_i)/\tau_n(v_i)$$

with functions $h_\infty(v_i), \tau_h(v_i), n_\infty(v_i), \tau_n(v_i)$ also specified in [1] and given in the appendix. We have introduced the parameter ϵ in (2) to emphasize that the h_i will be considered as slow variables in the upcoming analysis.

The architecture of synaptic connections in the network contributes to the form of the synaptic current I_{syn-e} . We will consider a single self-coupled cell and a pair of coupled cells. In both cases, let $I_{syn-e} = g_{syn-e} s_i(v_i - E_{syn-e})$ where

$$(4) \quad s'_i = \alpha_s(1 - s_i)s_\infty(v_j) - s_i/\tau_s,$$

with the function $s_\infty(v)$ and the constants α_s, τ_s specified in the appendix. In the self-coupled cell case, $i = j = 1$, while with a pair of coupled cells, $i, j \in \{1, 2\}$ with $j = 3 - i$.

2.2. Fast/slow decomposition and bifurcation structure for a single cell. For a single cell, let us omit the subscripts $i = j = 1$ on the dependent variables in the model. In system (2)–(3), $\epsilon/\tau_h(v) \ll 1/\tau_n(v)$ for all relevant v ; further, the evolution of h is much slower than that of v , as given by (1). Thus, it is natural to treat h as a parameter and to consider the bifurcation structure of the *fast subsystem* (1), (3), and (4) as h varies, a standard approach described, for example, in [20, 22]. Of course, in the full model, h does evolve, and the position of the h -nullcline determines the sign of the change in h at each location in phase space. Thus, the position of the h -nullcline relative to the bifurcation structures of the fast subsystem will contribute crucially to the dynamics of the network.

An example of the relevant bifurcation structures, for $(g_{tonic-e}, g_{syn-e}) = (0.2, 0)$, appears in Figure 1. For each fixed h , the fast subsystem, which we now take as (1), (3) since $g_{syn-e} = 0$, has 1, 2, or 3 critical points. The collection of all such points forms a curve in (h, v, n) -space, which we call the *fast nullcline* and denote by \mathcal{S} . The solid/dashed, S-shaped curve in Figure 1 is the projection of \mathcal{S} to (h, v) -space. Note that this nullcline has 3 branches over an intermediate range of h values. At an h value near 0.8, the middle and lower branches come together in a saddle-node bifurcation; we refer to the coalescence point as the *lower knee* of \mathcal{S} . Similarly, at an h value near -1.5 , the middle and upper branches coalesce in a saddle-node bifurcation at the *upper knee* of \mathcal{S} . The lower branch consists of stable critical points for (1), (3), while points on the middle branch are unstable saddles. Points on the upper branch are unstable for small h . As h increases, a subcritical Hopf bifurcation occurs along the upper branch of critical points, above which the critical points are stable. A family of unstable periodic orbits emanates from this bifurcation. This family meets with a second,

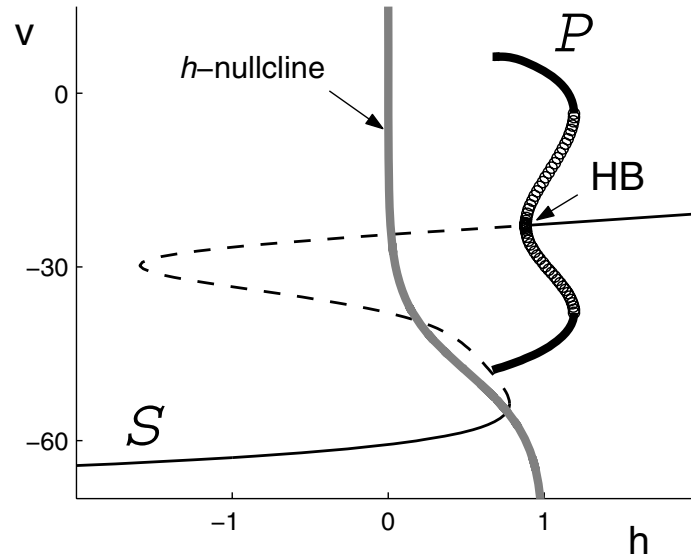


Figure 1. The bifurcation diagram for the fast subsystem (1), (3) with $(g_{tonic-e}, g_{syn-e}) = (0.2, 0)$, projected into (h, v) -space, along with the h -nullcline. The solid (dashed) black curve is the curve \mathcal{S} of stable (unstable) critical points of (1), (3) with h fixed at the levels indicated on the abscissa. A family of unstable periodic orbits, with maxima and minima labeled by open circles, emanates from \mathcal{S} in a Hopf bifurcation at the point marked HB . This family coalesces with the family of stable periodic orbits \mathcal{P} , with maxima and minima labeled by dark, thick curves, in a saddle-node bifurcation at h near 1.3. The thick grey curve shows the h -nullcline, namely, $h = h_{\infty}(v)$, where $h' = 0$.

outer family of periodics in a saddle-node bifurcation at a larger h value than the Hopf point. The outer periodics are stable and terminate in a homoclinic bifurcation as h decreases from the saddle-node. We will denote this outer family by \mathcal{P} . Finally, the h -nullcline, or *slow nullcline*, intersects \mathcal{S} in three places, which are critical points of the full system (1)–(3) (with $g_{syn-e} = 0$). The only stable critical point occurs on the fast nullcline’s lower branch and is attracting.

As $g_{tonic-e}$ increases, with $g_{syn-e} = 0$, it has three effects on the bifurcation diagram for the fast subsystem. Increasing $g_{tonic-e}$ causes the lower part of \mathcal{S} to move to smaller h values, causes \mathcal{P} to move to smaller h values, and causes the homoclinic point to move toward the lower knee of \mathcal{S} . These effects can be seen in the left column of Figure 2. These changes will have significant implications for the dynamics of the model cell. For comparison with the case of a coupled pair of cells, to be considered in section 3, it is important to note that we have numerically computed the saddle quantity [15] of the homoclinic point on the middle branch of \mathcal{S} for $g_{syn-e} = 0$ and a range of values of $g_{tonic-e}$. The saddle quantity remains negative over all relevant $g_{tonic-e}$, which implies that it is indeed a stable family of periodic orbits that emanates from each homoclinic point, and the saddle quantity decreases as $g_{tonic-e}$ increases, corresponding to the fact that the homoclinic point approaches the left knee of \mathcal{S} as $g_{tonic-e}$ increases (Figure 2).

Examples of voltage traces derived from the evolution of (1), (2), and (3), with $g_{syn-e} = 0$,

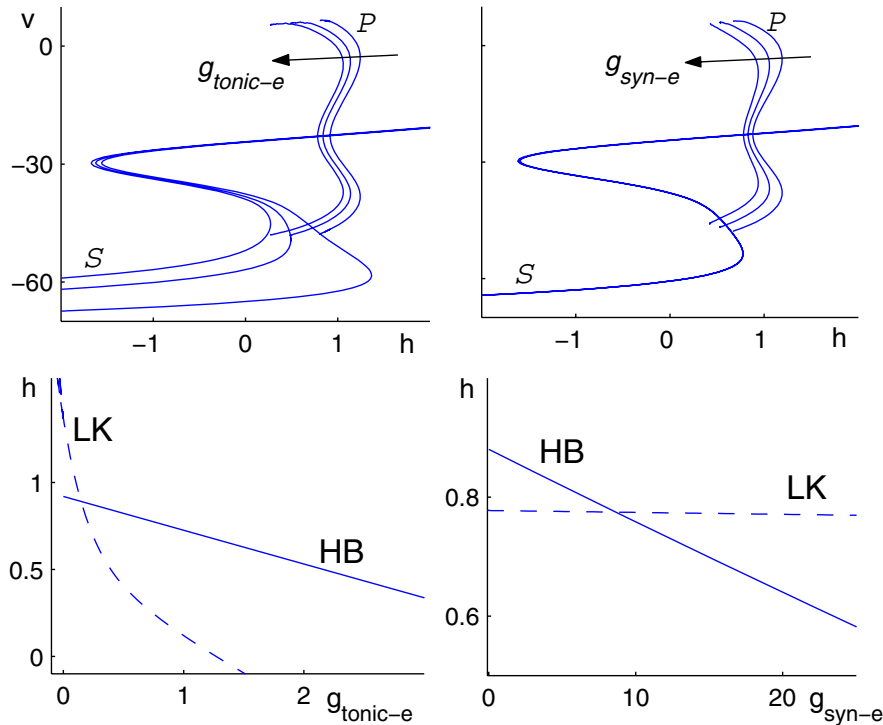


Figure 2. Dependence of the bifurcation structure of (1), (3), and (4) on $g_{\text{tonic-e}}$ and $g_{\text{syn-e}}$. The upper plots show curves of critical points and families of periodic orbits for varying values of $g_{\text{tonic-e}}$ and $g_{\text{syn-e}}$. Left: $g_{\text{tonic-e}} = 0, 0.4, 0.7, g_{\text{syn-e}} = 0$. Right: $g_{\text{tonic-e}} = 0.2, g_{\text{syn-e}} = 0, 4, 8$. Larger values correspond to more leftward structures. The bottom plots show how the positions of the lower knee (LK) and Hopf bifurcation point (HB) vary with $g_{\text{tonic-e}}$ (with $g_{\text{syn-e}} = 0$) and $g_{\text{syn-e}}$ (with $g_{\text{tonic-e}} = 0.2$), respectively. Note that the lower knee and indeed the entire curve of critical points are approximately invariant under changes in $g_{\text{syn-e}}$.

corresponding to a single uncoupled cell, are shown in Figure 3. Observe that as $g_{\text{tonic-e}}$ increases, the cell switches from quiescence to bursting to tonic spiking, as also shown in [2, 24]. In the quiescent case in Figure 3A, the trajectory is attracted to a stable critical point. In the bursting solution shown in Figure 3B, the trajectory spends some time on the lower branch of \mathcal{S} , where it is below the slow nullcline, such that h slowly increases. This is referred to as the *silent phase* of the solution. Although the two nullclines intersect very close to the lower knee, and it is difficult to discern in the figure, the intersection now occurs on the middle branch of \mathcal{S} . Thus, the trajectory can reach the lower knee and jump up to \mathcal{P} , and oscillations ensue, yielding the *active phase* of the solution. \mathcal{P} lies above the slow nullcline, so h decreases during the active phase. Finally, the trajectory approaches the homoclinic bifurcation where \mathcal{P} terminates, and it falls back to the lower branch. This form of bursting is called *square-wave bursting* and has been analyzed extensively in previous work [3, 20, 30, 31, 16].

Note that in the bottom panel of Figure 3B, there is an interval of h -values, extending on both sides of $h = 0.6$, for which the dynamics of the fast subsystem are bistable. Specifically, for each h in this range, there are a stable critical point on the lower branch of \mathcal{S} and a stable

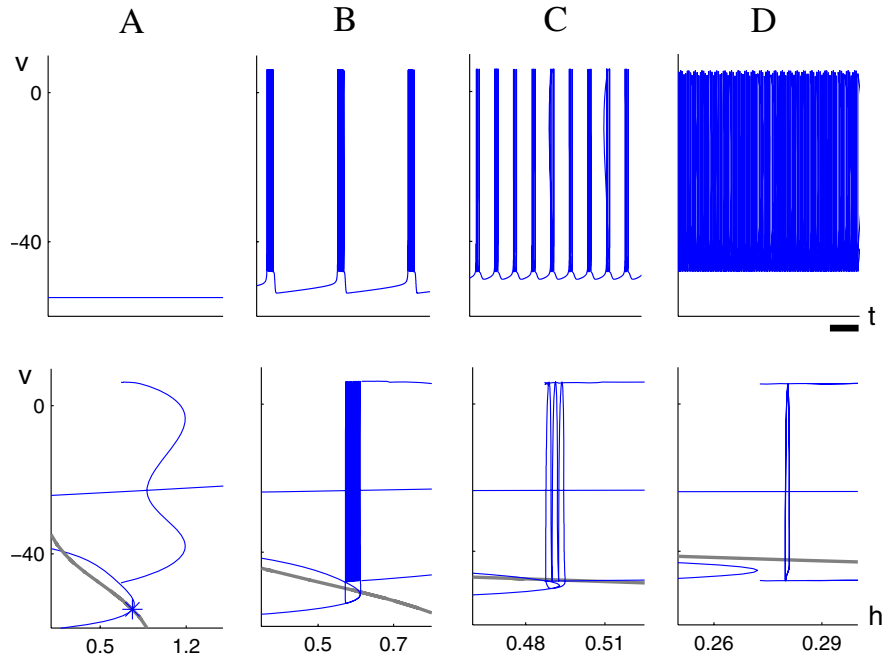


Figure 3. Voltage traces (top row) and bifurcation diagrams with superimposed trajectories and (grey) h -nullclines (bottom row). In all panels, $g_{syn-e} = 0$. The parameter $g_{tonic-e}$ takes values 0.2 (A - quiescence; stable critical point on the lower branch of \mathcal{S} denoted by *), 0.3 (B - bursting), 0.4 (C - bursting), and 0.7 (D - tonic spiking). In the top row, the scale bar corresponds to 2 seconds. Note the different h -axis scales in each panel in the bottom row.

periodic orbit from \mathcal{P} . The case in Figure 3C again represents square-wave bursting, but the range of bistable h values is much smaller than in Figure 3B. In this case, this leads to short bursts relative to Figure 3B. Finally, in Figure 3D, there is no region of bistability, and the trajectory is pinned in the vicinity of \mathcal{P} , such that tonic spiking results. Note from the bottom part of Figure 3D that the trajectory extends both above and below the slow nullcline (grey curve). While it is above (below) the slow nullcline, h decreases (increases). In the attracting state for the network, the net drift in h is zero, leading to the pinning and continuous spiking seen here [31].

Rather than varying $g_{tonic-e}$, we can keep $g_{tonic-e}$ fixed and consider the effect of varying g_{syn-e} on the bifurcation structure of the fast subsystem, now including (4), with $i = j = 1$, corresponding to a single self-coupled cell. Because of the influence of (4), changes in g_{syn-e} are not equivalent to changes in $g_{tonic-e}$. In particular, $s \approx 0$ along all branches of the fast nullcline \mathcal{S} , where v does not become much larger than -30 , due to the form and parameters of $s_\infty(v)$, as given in the appendix. Thus, increasing g_{syn-e} leaves the projection of \mathcal{S} to (h, v) -space largely unchanged, as seen in the right column of Figure 2. Increasing g_{syn-e} from 0 does cause \mathcal{P} to move to smaller h values, however, since s can become significant at the larger v values reached along \mathcal{P} . This shift widens the range of h values for which bistability occurs in the fast subsystem. Further, with its leftward motion, a greater part of this family lies below the slow nullcline, resulting in a decrease in the leftward drift during the

active phase of a burst. Eventually, this effect can cause pinning, corresponding to a transition from bursting to tonic spiking.

We explore the transitions between activity modes more systematically in the subsequent sections of the paper.

3. Analysis of transitions between modes of activity.

3.1. The transition from quiescence to bursting. As noted in section 2, a cell or network of identical cells is quiescent when the fast and slow nullclines have an intersection on the lower branch of \mathcal{S} . Given a network in the quiescent state, bursting can be induced by increasing $g_{tonic-e}$. Indeed, as also observed in [2] (see Figure 2 of [2], also reproduced in Figure 18 below), the value of $g_{tonic-e}$ at which the switch from quiescence to bursting occurs, namely, $g_{tonic-e} \approx 0.26$, depends only very weakly on the value of g_{syn-e} .

The mechanism underlying the switch from quiescence to bursting is that as $g_{tonic-e}$ increases, \mathcal{S} , and in particular its lower knee, moves leftward in the (h, v) -plane, to smaller h -values, as mentioned in section 2 (Figure 2). Since the slow nullcline is independent of $g_{tonic-e}$, this trend causes the lowest v intersection of the nullclines (call it p) to transition from lying on the lowest branch of \mathcal{S} to lying on the middle branch of \mathcal{S} , by passing through the lower knee of \mathcal{S} . In this transition, an eigenvalue of the linearization of (1)–(4) about p crosses from the negative real axis to the positive real axis, such that on the middle branch, p is an unstable critical point of (1)–(4). Trajectories starting in the silent phase now flow past the lower knee of \mathcal{S} and are attracted to the family of periodic orbits \mathcal{P} . Bursting, rather than tonic spiking, results from the transition for the parameter values of interest due to a combination of two factors seen in Figure 3B; there is always bistability between the lower branch and \mathcal{P} when this transition occurs, and there is a net leftward drift in h during the active phase. Finally, the transition is relatively independent of g_{syn-e} because, as noted in section 2 (e.g., Figure 2, right top panel), g_{syn-e} has little impact on the position of \mathcal{S} and hence on the position of the critical point p .

3.2. The transition from bursting to tonic spiking in a self-coupled cell. The transition from bursting to tonic spiking is much more complex than that from quiescence to bursting. In fact, there are several different mechanisms underlying the transition from bursting to tonic spiking, depending on parameter values. Here we will briefly return to the simplest case of a single self-coupled cell, as considered in subsection 2.2; note that this case is also equivalent to a pair of coupled cells that are completely synchronized. As we shall discuss in the subsequent subsections, the completely synchronized solution is generally unstable with respect to the full system, and coupled cells fire spikes that are out of phase in the stable bursting and tonic spiking solutions. However, the progression in analysis presented in this and subsequent subsections will illustrate the precise way in which asynchrony between cells within the spiking phase can fundamentally alter the fast/slow bifurcation structure and be a significant ingredient in determining the model's dynamic range of bursting.

Consider a single, self-coupled cell, which satisfies (1)–(4) with (v_i, h_i, n_i, s_i) replaced by (v, h, n, s) . As in subsection 3.1, we analyze this system using fast/slow analysis with h as the slow variable, and representative bifurcation diagrams are shown in Figure 2. Define the h -nullsurface $\mathcal{G} = \{(v, h, n, s) : h = h_\infty(v)\}$ and let $p = \mathcal{G} \cap \mathcal{S}$ as in subsection 3.1. Note

that (1)–(4) exhibits square-wave bursting if there is an interval of h -values where the fast subsystem exhibits bistability and p lies between the lower knee of \mathcal{S} and the homoclinic point $\mathcal{P} \cap \mathcal{S}$. Alternatively, if p lies at a smaller h -value than that of the homoclinic point on the middle branch of \mathcal{S} , then, in the limit $\epsilon \rightarrow 0$ in (2), system (1)–(4) will exhibit tonic spiking. Thus, as demonstrated in [31], the transition from square-wave bursting to tonic spiking, in the limit $\epsilon \rightarrow 0$, occurs when the homoclinic point on the middle branch of fixed points crosses \mathcal{G} .

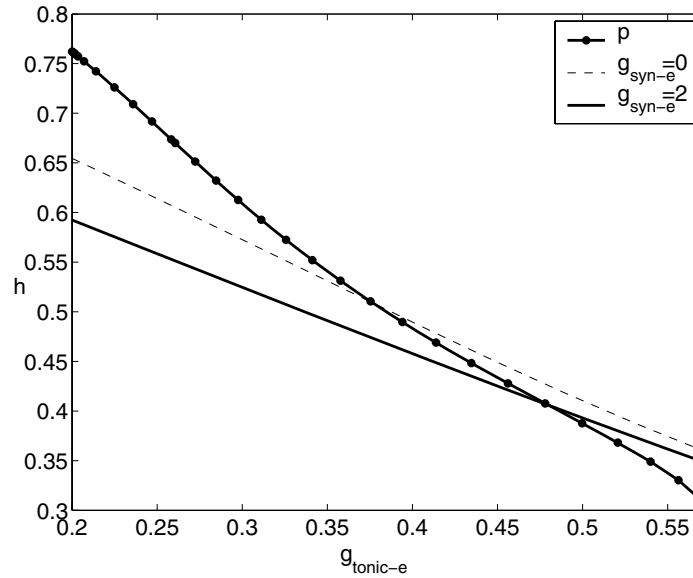


Figure 4. The curve of fixed points p of (1)–(4), together with the curves of homoclinic points $\mathcal{P} \cap \mathcal{S}$ of the fast subsystem (1), (3), and (4) for $g_{syn-e} = 0$ and $g_{syn-e} = 2$, as a function of $g_{tonic-e}$. The intersections of these curves yield the values of $g_{tonic-e}$ at which the transition from bursting to tonic spiking is predicted to occur, based on a fast/slow decomposition of the single self-coupled cell. Note that although p switches from the lower branch of \mathcal{S} to the middle branch at $g_{tonic-e} \approx 0.26$, the h -value of p is a monotonically decreasing function of $g_{tonic-e}$, because all of \mathcal{S} moves toward smaller h values as $g_{tonic-e}$ increases.

As illustrated in the examples in Figure 2 and particularly in Figure 4, the homoclinic point for the self-coupled cell lies at smaller h than that for the uncoupled cell. Thus, $g_{tonic-e}$ must be increased more for \mathcal{G} to cross the curve of homoclinic points in the self-coupled case, and the transition to tonic spiking occurs at a higher value of $g_{tonic-e}$ than for the uncoupled cell; that is, a self-coupled cell has a larger dynamic range of bursting oscillations than an uncoupled cell has.

To finish this analysis, we use XPPAUT [9] to follow the curve in $(g_{tonic-e}, g_{syn-e})$ parameter space where \mathcal{G} intersects the homoclinic point $\mathcal{P} \cap \mathcal{S}$. This generates a transition curve, shown in Figure 5, with a shape that qualitatively matches that in Figure 2 of [2] (see Figure 18 below). There is a significant quantitative difference between the two results, however, with the curve in Figure 5 substantially underestimating the extent of the bursting region. Thus, we conclude that the dynamics of a single self-coupled cell, while interesting in their own right, do not capture the complexity of the bursting and spiking behaviors in the

pre-BötC model with multiple, synaptically coupled cells.

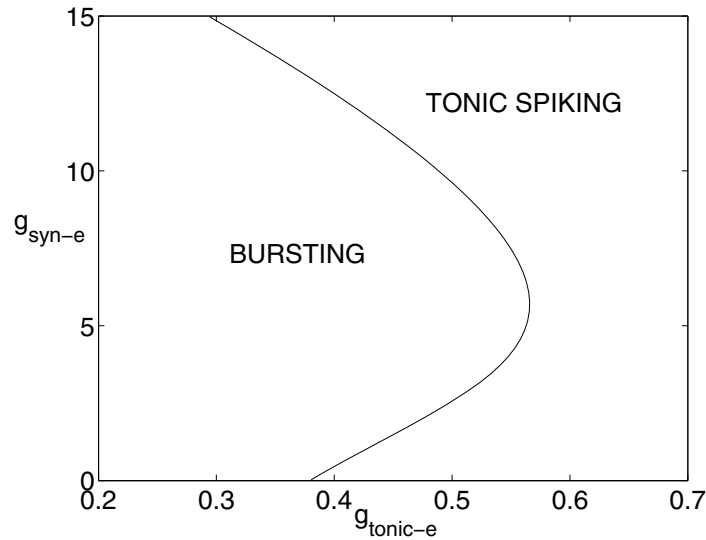


Figure 5. The transition curve $(\mathcal{G} \cap \mathcal{P} \cap \mathcal{S})$ between bursting (to the left) and tonic spiking (to the right) predicted by analysis of a single self-coupled cell. This curve significantly underestimates the extent of the bursting region.

3.3. The transition from bursting to spiking in coupled cells with $h_1 = h_2$. In the previous section, we assumed that the cells were completely synchronized and concluded that this does *not* accurately predict the full increase in dynamic range for the coupled system. Figure 6 illustrates why this should not be surprising. Here we show the voltage traces of the two cells for $(g_{\text{tonic-e}}, g_{\text{syn-e}}) = (0.5, 8)$. Note that while the cells appear to burst together, their spikes fire out-of-phase. We must, therefore, extend the fast/slow analysis to the case in which we consider asynchronous spiking. This will be done in two steps. In this section, we assume that the slow variables h_1 and h_2 are equal; we can then perform the fast/slow analysis with a single slow variable, $h = h_1 = h_2$. As we shall see, this assumption leads to an accurate prediction for the transition to tonic spiking for large values of $g_{\text{syn-e}}$ (see Figure 7). Moreover, the resulting bifurcation structure has some rather novel features not seen in the analysis of the self-coupled cell. For moderate and low values of $g_{\text{syn-e}}$, we can no longer assume that $h_1 = h_2$; these must be considered as separate slow variables (Figure 7). The two-slow-variable analysis will be carried out in the next subsection.

Denote the system of eight equations, consisting of (1)–(4) taken with both $i = 1$ and $i = 2$, by $(1)_i$ – $(4)_i$. Figure 8 shows an example of the bifurcation diagram generated by the fast subsystem consisting of the six equations $(1)_i$, $(3)_i$, $(4)_i$ with $h_1 = h_2 = h$ as the single bifurcation parameter. This diagram is projected onto the (h, v_1) -plane. Note that two families of periodic orbits emanate from the single curve of equilibria \mathcal{S} in distinct subcritical Hopf bifurcations. As we move from right to left along the h -axis, starting above both Hopf points, the critical points on \mathcal{S} are stable. They lose stability in the first Hopf bifurcation, which gives rise to an unstable family of periodic orbits, labeled as \mathcal{IP} in Figure 8 and consisting

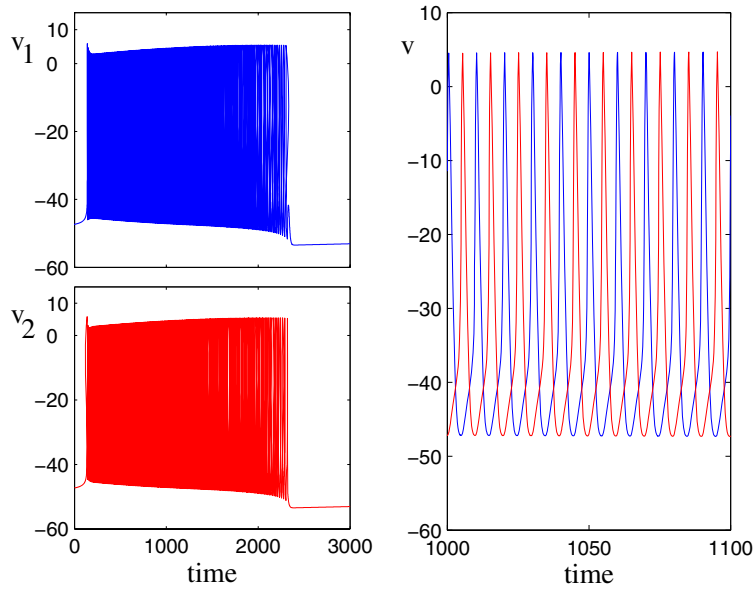


Figure 6. Bursting solutions of the full model (1)–(4). Here, $(g_{tonic-e}, g_{syn-e}) = (0.5, 8)$. The left panel shows that the bursts appear to be synchronized. The right panel shows that the spikes actually occur in antiphase.

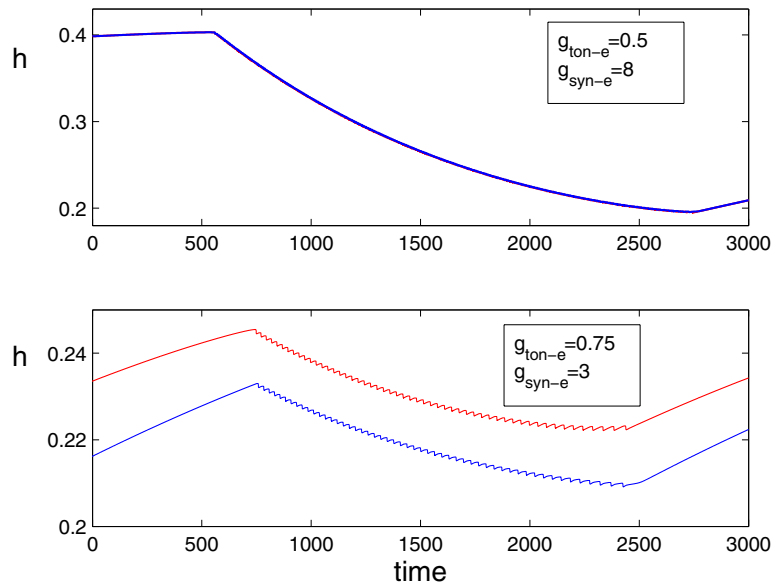


Figure 7. Plots of h_1 (red) and h_2 (blue) as functions of time during a single burst cycle. If g_{syn-e} is large (top), then $h_1 \approx h_2$, while for moderate or low values of g_{syn-e} (bottom), we cannot assume that $h_1 \approx h_2$.

of in-phase oscillations, as h is decreased. Both branches of periodics in \mathcal{IP} , which merge at a saddle-node bifurcation, are unstable with respect to the fast subsystem, except possibly for the outer branch in some relatively small neighborhood of the saddle-node bifurcation. The second family of periodics (call it \mathcal{AP}) occurs at lower h and corresponds to antiphase oscillations. This family consists of three branches. The branch that emanates from the subcritical Hopf consists of unstable limit cycles. This branch terminates at a saddle-node of periodic orbits, at $h = h_R$ in Figure 8, where it coalesces with a second branch of periodic orbits. This second branch is *stable*, at least away from a relatively small neighborhood of the saddle-node bifurcation. It will be very important in the analysis and we label it as \mathcal{AP}_S . This branch terminates in another saddle-node bifurcation of periodic orbits, at $h = h_L$ in Figure 8, where it coalesces with a *third* branch of unstable periodics. The third branch terminates in an orbit homoclinic to the middle branch of \mathcal{S} . (Note that the upper branch corresponding to this family lies very close to that of \mathcal{AP}_S , and hence cannot be distinguished at the scale shown in Figure 8.) A similar emergence of antiphase and in-phase periodic orbit families is also seen when diffusive coupling is introduced between square-wave bursters derived from a model for bursting in pancreatic β -cells [25].

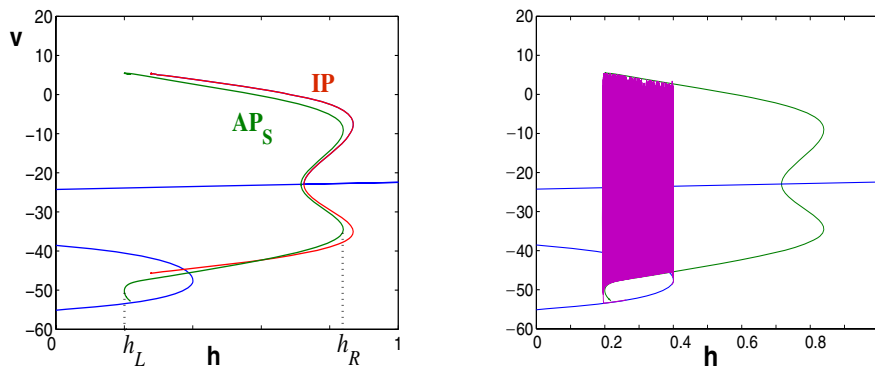


Figure 8. Bifurcation structure of the fast subsystem for $(g_{tonic-e}, g_{syn-e}) = (0.5, 8)$. Here we assume that $h = h_1 = h_2$ is the bifurcation parameter. The branch of fixed points \mathcal{S} is shown in blue. There are two branches of periodic orbits; in-phase solutions (\mathcal{IP}) are shown in red, while antiphase solutions are shown in green. The stable portion of the antiphase branch is denoted as \mathcal{AP}_S and exists on the interval $[h_L, h_R]$. The projection of a bursting solution (purple) onto this bifurcation diagram is shown in the right panel. Note that the active phase ends at a saddle-node of periodic solutions of the fast subsystem.

Remark 3.1. For h values below both Hopf bifurcations, linearization of the 6-dimensional fast subsystem around each critical point on the upper branch of \mathcal{S} yields four eigenvalues with positive real parts. As \mathcal{S} is followed around the upper knee, although all four unstable eigenvalues become real, *two* of these cross through the origin, by symmetry. Similarly, the other two unstable eigenvalues stabilize at the lower knee, such that the critical points on the lower branch of \mathcal{S} are indeed stable.

Remark 3.2. Numerical calculations suggest that when the fast subsystem is linearized about the homoclinic point at which the third branch of \mathcal{AP} terminates, which lies on the middle branch of \mathcal{S} , the unstable pair of eigenvalues has larger magnitude than that of the leading stable eigenvalues. Because the multiplicity of these eigenvalues comes from symmetry

and not degeneracy, the saddle quantity [15] is relevant, and based on this, the periodic orbits on this third branch are unstable, as we observe in our bifurcation diagrams and direct numerical simulations. This differs from the standard square-wave bursting scenario, seen in the case of the single, self-coupled cell in subsection 2.2, in which the leading stable eigenvalue has larger magnitude than the unstable eigenvalue and stable periodic orbits emerge from the homoclinic point as h is increased.

Figure 8 also shows the projection of the bursting solution shown in Figure 6 onto the fast subsystem bifurcation diagram. As usual, the silent phase lies along the lower branch of \mathcal{S} and the active spiking phase begins when the trajectory reaches the lower knee of \mathcal{S} . During the active phase, the trajectory lies close to $\mathcal{AP}_{\mathcal{S}}$ and the active phase ends when the trajectory reaches the saddle-node of periodics. Note that this bifurcation structure no longer corresponds to square-wave bursting, where spiking ends at a homoclinic orbit, but rather represents a different bursting class (see also [11, 27, 4, 26]). We have, therefore, demonstrated that synaptic coupling of cells leads to a change in the class of bursting activity that occurs. As we demonstrate below, this will contribute to the fact that the coupled system has an increased dynamic range. A 3-dimensional caricature of this induced form of bursting is illustrated in Figure 9. We shall refer to this bursting class, which is called fold/fold cycle bursting in [11], as *top hat bursting*.

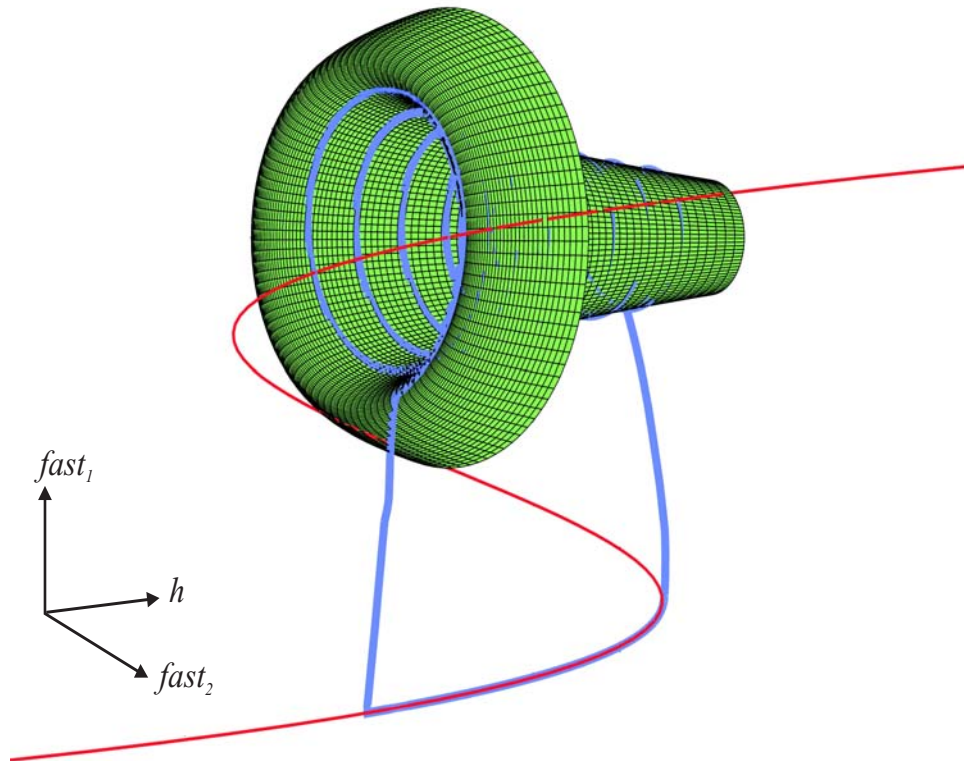


Figure 9. A schematic illustration of a top hat burster. A similar top hat structure would arise from a system with two fast variables and one slow variable or from a projection of a higher-dimensional system, such as we consider, onto two fast dimensions and one slow dimension.

Top hat bursters have several important features that distinguish them from square-wave bursters. The active phase of a square-wave burster ends at a homoclinic orbit. For this reason, the spike frequency becomes small at the end of each burst. For top hat bursters, the active phase ends at a saddle-node of limit cycles. Hence, the spike frequency approaches some fixed value, bounded away from zero, at the termination of burst activity.

A second difference between square-wave and top hat bursting is related to the transition to tonic spiking as a parameter, such as $g_{\text{tonic-e}}$, is varied. Recall that for a square-wave burster, this transition takes place as the homoclinic point crosses the slow nullsurface, denoted by \mathcal{G} earlier. For top hat bursters, this transition arises from a very different mechanism. To understand this new mechanism, we use singular perturbation methods to reduce the full system of (1)_{*i*}–(4)_{*i*} to a reduced system for just the slow variables. Since we are now assuming that $h_1 = h_2$, this will lead to a reduction of the full model to a single equation. The reduction is carried out separately for the silent and active phases.

While in the silent phase, the solution lies close to the lower branch of \mathcal{S} and we invoke a steady state approximation. That is, introduce the slow time variable $\tau = \epsilon t$ in (1)_{*i*}–(4)_{*i*} and then set $\epsilon = 0$. The right hand sides of (1)_{*i*}, (3)_{*i*}, and (4)_{*i*} then become zero and we may solve for fast variables (v_i, n_i, s_i) , $i = 1, 2$, in terms of h . While there are multiple possible solutions, we choose that with the smallest v , corresponding to the silent phase. As a result, since we use the same h for $i = 1$ and $i = 2$, we obtain $(v_1, n_1, s_1) = (v_2, n_2, s_2)$ in the silent phase. After substituting $v_1 = v_2$ into (2), we obtain a single equation for the evolution of h in the silent phase.

For the active phase, we use the method of averaging. Suppose that $\mathcal{AP}_{\mathcal{S}}$ exists for $h_L \leq h \leq h_R$ (Figure 8). For $h_L \leq h \leq h_R$, let $(v_i(t, h), n_i(t, h), s_i(t, h))$, $i = 1, 2$, be the corresponding antiphase periodic orbit of the fast subsystem and assume that its period is $T(h)$. Then, in the limit $\epsilon \rightarrow 0$, the evolution of h during the active phase is governed by the averaged equation

$$(5) \quad \dot{h} = \frac{1}{T(h)} \int_0^{T(h)} (h_{\infty}(v_i(t, h)) - h) / \tau_h(v_i(t, h)) dt \equiv a(h).$$

Here, differentiation is with respect to τ . We may use v_1 or v_2 in (5), since we are assuming that $h_1 = h_2$ and we are therefore integrating over a common periodic orbit, belonging to the stable family $\mathcal{AP}_{\mathcal{S}}$, for $i = 1$ and $i = 2$, although the cells may be out of phase along the orbit.

Now the system exhibits bursting if $a(h) < 0$ for all $h \in (h_L, h_R)$. In this case, the solution drifts to the left while oscillating along $\mathcal{AP}_{\mathcal{S}}$. The onset of tonic spiking occurs at the minimal value of $g_{\text{tonic-e}}$ for which there exists a stable fixed point of (5) in $[h_L, h_R]$ that has the lower knee of \mathcal{S} in its basin of attraction. In theory, such a fixed point could arise at the saddle-node of periodic orbits at h_L (Figure 8), yielding a unique tonic spiking solution, or it could first appear via a double zero of $a(h)$ in (h_L, h_R) , leading to a saddle-node bifurcation of tonic spiking solutions, one stable and one unstable, as $g_{\text{tonic-e}}$ increases [27, 4, 26]. (Recall that we only evaluate (5) along periodic orbits in $\mathcal{AP}_{\mathcal{S}}$, ignoring possible unstable tonic spiking solutions corresponding to the unstable branch of periodic orbits that is also born at $h = h_L$.) Our simulations show that $a(h)$ is a monotone decreasing function on $[h_L, h_R]$ for each fixed $g_{\text{tonic-e}}$. Thus, bursting occurs, with $a(h) < 0$ on $[h_L, h_R]$, for sufficiently small $g_{\text{tonic-e}}$,

and the transition from bursting to tonic spiking happens at the minimal $g_{\text{tonic-e}}$ such that $a(h_L) = 0$. An example is given in Figure 10.

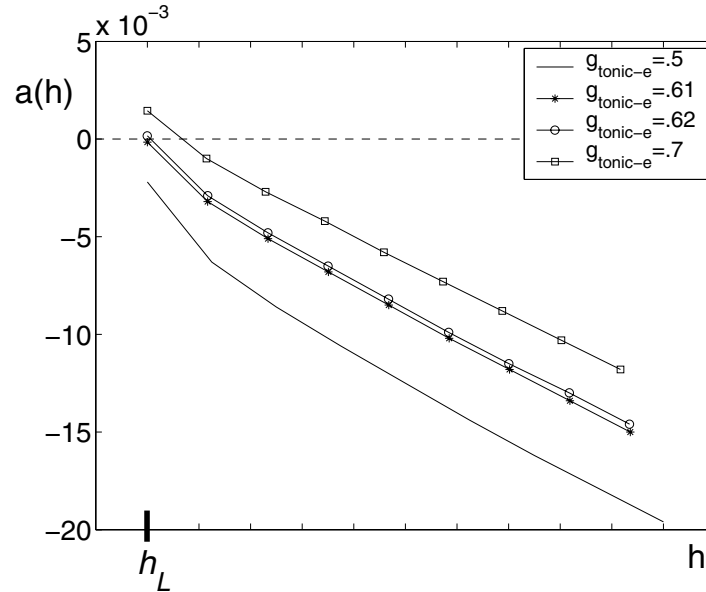


Figure 10. The function $a(h)$ plotted over $[h_L, h_{LK}]$ for $g_{\text{syn-e}} = 8$ and several $g_{\text{tonic-e}}$ values, where h_{LK} is the h -value for the lower knee of \mathcal{S} . For all $g_{\text{tonic-e}}$, $a(h)$ remains monotone decreasing. As $g_{\text{tonic-e}}$ increases from 0.61 to 0.62, a zero of $a(h)$ occurs at $h = h_L$, and this zero moves away from h_L toward larger h -values as $g_{\text{tonic-e}}$ increases further. Note that the actual values of h_L, h_{LK} depend on $g_{\text{tonic-e}}$, and hence we omit numerical labels from the h -axis; all of the curves shown have been aligned according to their respective h_L values for comparison.

The criterion $a(h_L) = 0$ gives an accurate prediction for the value of $g_{\text{tonic-e}}$ at which the transition from bursting to tonic spiking occurs for large values of $g_{\text{syn-e}}$. For small and moderate values of $g_{\text{syn-e}}$, this curve does not match the actual transition; it severely underestimates the increase in dynamic range of bursting activity. The reason for this discrepancy is that, for small and moderate values of $g_{\text{syn-e}}$, the behavior of the full system is inconsistent with the assumption that $h_1 = h_2$. We must, therefore, extend our fast/slow analysis to the case of two slow variables.

3.4. The transition from bursting to tonic spiking in the full model for two coupled cells.

3.4.1. Using slow averaged dynamics in the oscillation region to analyze activity states.

The previous subsections demonstrate that to capture the full picture of the dynamic range of bursting for two coupled pre-BötC cells, it is necessary to consider the full four-equation model (1)–(4) for each cell. Again, there is a natural fast/slow decomposition, achieved by taking h_1, h_2 as slow variables; below, we refer to the *fast subsystem* to mean the other six equations with h_1, h_2 frozen. Rather than visualizing fast subsystem bifurcation structures, we will now consider dynamics projected to the (h_1, h_2) -plane.

To start, fix $(g_{\text{tonic-e}}, g_{\text{syn-e}})$ and note that for some pairs (h_1, h_2) , the fast subsystem will

support regular, stable tonic spiking, while for others, such sustained oscillations will not exist. We can use direct simulation of the fast subsystem (e.g., fixing h_2 , varying h_1 systematically, and then repeating for a different h_2), to estimate a boundary curve for the *oscillation region* \mathcal{O} in (h_1, h_2) -space, such that for (h_1, h_2) -values below this curve, regular, stable oscillations do not exist for the fast subsystem. In what follows, we denote this boundary curve as \mathcal{B} .

Remark 3.3. We use the term regular oscillations to refer specifically to periodic solutions in which the two cells fire in alternation, with constant interspike intervals. We will return to the issue of regular versus irregular oscillations of the fast subsystem later in this subsection.

We use averaging to reduce the full system to a system of two equations for just the slow variables. For $g(v, h) \equiv (h_\infty(v) - h)/\tau_h(v)$, the reduced system can be written as

$$(6) \quad \begin{aligned} \dot{h}_1 &= \frac{1}{T(h_1, h_2)} \int_0^{T(h_1, h_2)} g(v_{1_p}(h_1, h_2; t), h_1) dt \equiv a_1(h_1, h_2), \\ \dot{h}_2 &= \frac{1}{T(h_1, h_2)} \int_0^{T(h_1, h_2)} g(v_{2_p}(h_1, h_2; t), h_2) dt \equiv a_2(h_1, h_2), \end{aligned}$$

where $(h_1, h_2) \in \mathcal{O}$, $T(h_1, h_2)$ is the period of the fast subsystem periodic orbit for this choice of (h_1, h_2) , and v_{1_p}, v_{2_p} are the time courses of v_1, v_2 around the orbit, which both depend on both h_1 and h_2 , since the orbit itself does. Note that tonic spiking corresponds to a stable fixed point of (6). In fact, as we now demonstrate, the complete transition from bursting to tonic spiking for the full system can be understood by analyzing the phase planes generated by (6).

Figure 11 illustrates phase planes of (6) with $g_{syn-e} = 3$ and four values of $g_{tonic-e}$. Note that for this value of g_{syn-e} , the analysis in the preceding section, in which we assumed that $h_1 = h_2$, does not give an accurate prediction for when the transition from bursting to spiking takes place for the full system. In each panel of Figure 11, the black curve represents \mathcal{B} , the boundary of the oscillation region. When a bursting solution crosses \mathcal{B} , it falls back to the silent phase (not shown in the figure), and spiking activity stops until a subsequent burst cycle begins. The red and blue curves in Figure 11 are numerically computed averaged nullclines, namely, $\mathcal{A}_1 = \{(h_1, h_2) : a_1(h_1, h_2) = 0\}$ and $\mathcal{A}_2 = \{(h_1, h_2) : a_2(h_1, h_2) = 0\}$. Fixed points of (6) are given by the intersections of these nullclines, and one can usually determine the stability of the fixed points by considering the nullcline configuration. Note that to estimate the positions of \mathcal{A}_1 and \mathcal{A}_2 , we simulate the fast subsystem $(1)_i, (3)_i, (4)_i$. This consists of fixing h_2 and systematically varying h_1 to identify locations where either $a_1(h_1, h_2)$ or $a_2(h_1, h_2)$ is sufficiently close to zero, repeating the process for each h_2 on a partition of the relevant h_2 range, which corresponds to the interior of the region \mathcal{O} as determined by the location of \mathcal{B} .

In Figure 11A, $g_{tonic-e} = .57$. Note that \mathcal{A}_1 and \mathcal{A}_2 are not present in \mathcal{O} , and therefore both \dot{h}_1 and \dot{h}_2 remain negative along every trajectory in \mathcal{O} . Hence, every solution of the averaged slow equations (6) must eventually leave \mathcal{O} through \mathcal{B} and the full system $(1)_i$ – $(4)_i$ exhibits bursting. The bursting is symmetric in the sense that trajectories of (6) converge to the line $\mathcal{L} \equiv \{(h_1, h_2) : h_1 = h_2\}$ over successive burst cycles and oscillate symmetrically about it while in \mathcal{O} , and hence we refer to this as *symmetric bursting*. In general, this is a top hat burster and can be analyzed using the one slow variable analysis described in the preceding section.

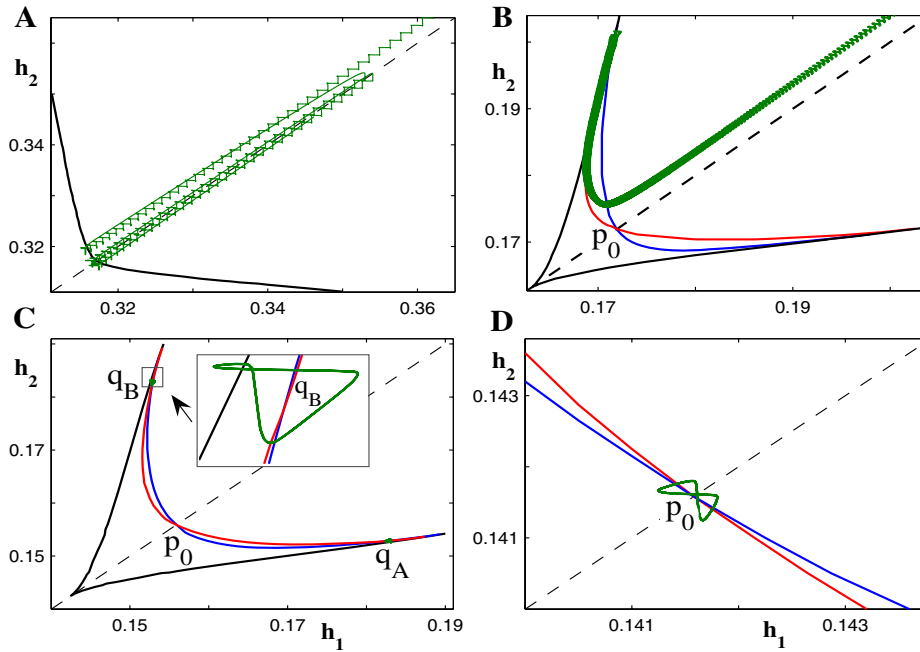


Figure 11. Averaged phase planes, corresponding to (6), with superimposed trajectories of (1)_i–(4)_i, for $g_{\text{syn-e}} = 3$. Throughout this figure, the jump-down curve \mathcal{B} is solid black, the nullclines $\mathcal{A}_1, \mathcal{A}_2$ are red and blue, respectively, the symmetry axis \mathcal{L} is dashed black, and trajectories are green. (A) For $g_{\text{tonic-e}} = .57$, \dot{h}_1, \dot{h}_2 are negative everywhere in the oscillatory region \mathcal{O} . Thus, every solution of the averaged equations leaves the oscillatory region \mathcal{O} through \mathcal{B} and the system exhibits symmetric bursting. The trajectories here correspond to the flow of (1)_i–(4)_i during the active phases of several bursts only, with the silent phases omitted. (B) For $g_{\text{tonic-e}} = .83$, there is an unstable fixed point p_0 in \mathcal{O} where the averaged nullclines intersect. The system exhibits asymmetric bursting. Again, the trajectory shown is from the active phase of bursting. (C) For $g_{\text{tonic-e}} = .87$, the averaged nullclines intersect at three fixed points in \mathcal{O} , namely, p_0 , which is still unstable, and q_A, q_B , which are stable. The system exhibits asymmetric tonic spiking. An asymmetric tonic spiking solution is shown in green; similar solutions exist near q_A . (D) For $g_{\text{tonic-e}} = .91$, p_0 is a stable fixed point and the system exhibits symmetric spiking. Here \mathcal{B} is not visible since it lies at smaller (h_1, h_2) values than those shown in this plot.

In Figure 11B, $g_{\text{tonic-e}} = .83$ and the full system still exhibits bursting. However, the slow system (6) now has a fixed point, denoted by p_0 in Figure 11B, inside of \mathcal{O} . Indeed, this fixed point enters \mathcal{O} through the intersection point of \mathcal{B} with the line $\mathcal{L} \equiv \{(h_1, h_2) : h_1 = h_2\}$ as $g_{\text{tonic-e}}$ increases. Using the fact that the slope of the h_2 -nullcline at p_0 is more negative than the slope of the h_1 -nullcline there and the reflection symmetry of (6), we have $n_b \equiv \partial \dot{h}_1 / \partial h_2 = \partial \dot{h}_2 / \partial h_1 < n_s \equiv \partial \dot{h}_1 / \partial h_1 = \partial \dot{h}_2 / \partial h_2 < 0$. Thus, the eigenvalues $n_s \pm |n_b|$ of the linearization of (6) about p_0 have opposite signs, such that p_0 is an unstable saddle of (6). The stable manifold of p_0 lies along the line \mathcal{L} , while each solution of (6) that does not begin along \mathcal{L} must eventually leave the oscillation region through \mathcal{B} , after crossing through \mathcal{A}_1 and \mathcal{A}_2 and experiencing a change in the sign of \dot{h}_1 and \dot{h}_2 , respectively. As a result, the full system generically exhibits bursting oscillations. We shall refer to this as *asymmetric bursting* since $h_1 \neq h_2$ along the solution. We note that it is essential here to consider two-slow-variable

analysis. If, as in the preceding section, we assumed that $h_1 = h_2$, then we would incorrectly predict that the full system exhibits tonic spiking as soon as p_0 enters \mathcal{O} , which occurs at significantly smaller $g_{tonic-e}$ than the actual spiking onset. That is, p_0 is stable with respect to solutions of (6) that lie along the stable manifold \mathcal{L} . This explains why the analysis in the preceding section does not accurately predict the full dynamic range of rhythmic bursting oscillations. Further, the fact that no saddle-node bifurcation gives rise to critical points of (6) along \mathcal{L} , away from \mathcal{B} , as $g_{tonic-e}$ increases corroborates our earlier claim that no saddle-node bifurcation occurs in the fixed points of (5).

For Figure 11C, we set $g_{tonic-e} = .87$. While there is still an unstable fixed point $p_0 \in \mathcal{O}$, the averaged nullclines \mathcal{A}_1 and \mathcal{A}_2 now intersect at two new fixed points, labeled as q_A and q_B , in the oscillatory region \mathcal{O} . These fixed points are stable, as can be seen from the configuration of the nullclines, and they represent tonic spiking of the full system. We say that this is *asymmetric tonic spiking* because $h_1 \neq h_2$ at q_A and q_B ; that is, the stable fixed points do not lie along the axis of symmetry \mathcal{L} .

Finally, suppose that $g_{tonic-e} = .91$. In this case, as shown in Figure 11D, p_0 is a stable fixed point of (6) and the full system exhibits symmetric tonic spiking. The configuration of the nullclines \mathcal{A}_1 and \mathcal{A}_2 at p_0 has now switched from the previous cases. That is, as we increase $g_{tonic-e}$ from .87 to .91, a pitchfork bifurcation occurs. In this bifurcation, the stable fixed points q_A and q_B come together at p_0 , and p_0 switches from being a saddle to being a stable node. Figure 11D also shows an example of how a tonic spiking trajectory oscillates symmetrically about p_0 . It is important to note that, even in these *symmetric tonic spiking* solutions, we expect v_1 and v_2 to be antiphase. This can be checked for small g_{syn-e} by calculating the H -function [13, 10]. The functions $H(\phi)$ and $H_{odd}(\phi) \equiv (H(\phi) - H(-\phi))/2$ for $g_{tonic-e} = 1.05$ and $g_{syn-e} = 1$ appear in Figure 12. A zero of $H_{odd}(\phi)$ represents a phase-locked, periodic solution of the full system, which is stable (unstable) if the derivative of H_{odd} is positive (negative) there. Since the phase shift in a solution is given by the value of ϕ at which the corresponding zero of $H_{odd}(\phi)$ occurs, Figure 12 predicts that v_1, v_2 will be exactly antiphase for this $(g_{tonic-e}, g_{syn-e})$ (see also Figure 6).

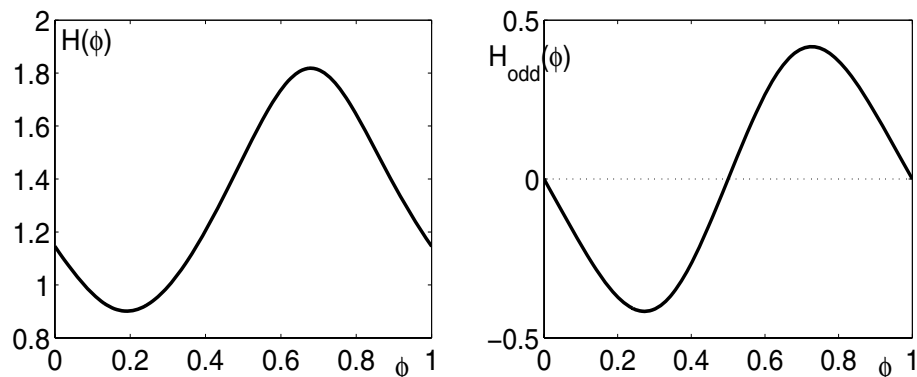


Figure 12. H -function and its odd part H_{odd} for $g_{tonic-e} = 1.05$ and $g_{syn-e} = 1$. Since $H_{odd}(0.5) = 0$ and $H'_{odd}(0.5) > 0$, the antiphase symmetric spiking solution is predicted to be stable.

Remark 3.4. We have also numerically computed the H -function for symmetric bursting

for particular values of $g_{tonic-e}, g_{syn-e}$. The results agree with our analysis, showing that spikes are out of phase within the stable solution. The results also suggest that a completely antiphase solution, in which the cells take turns bursting, should also be stable. However, it is important to note that this calculation is relevant in the weak coupling limit. Our simulations show that such antiphase bursting solutions indeed may stably exist, but only for extremely small g_{syn-e} . Further consideration of antiphase bursting solutions is outside of the scope of this work.

Figure 13 shows regions in $(g_{tonic-e}, g_{syn-e})$ parameter space where the full coupled system (1)_{*i*}–(4)_{*i*} is predicted to exhibit symmetric bursting (SB), asymmetric bursting (AB), asymmetric spiking (AS), and symmetric spiking (SS). As seen above, the SB region corresponds to the absence of fixed points in \mathcal{O} , and the symmetry expected here refers to an approximate equality of h_1 and h_2 . We have not yet justified why solutions in SB should, in general, have $h_1 \approx h_2$, however, and this is discussed in subsection 3.4.3 in the context of synchronization of bursts. The blue curve corresponds to when the fixed point p_0 first appears in \mathcal{O} as $g_{tonic-e}$ is varied, representing the transition from SB to AB. This is where the one-slow variable analysis described in the previous section predicts that there should be the transition from bursting to tonic spiking. The green curve corresponds to the transition from AB to AS. Recall that this occurs when the additional intersections of the averaged nullclines \mathcal{A}_1 and \mathcal{A}_2 , namely, the stable fixed points q_A and q_B , appear in \mathcal{O} . The red curve corresponds to the transition to SS. This corresponds to the occurrence of a pitchfork bifurcation for the slow averaged equations (6).

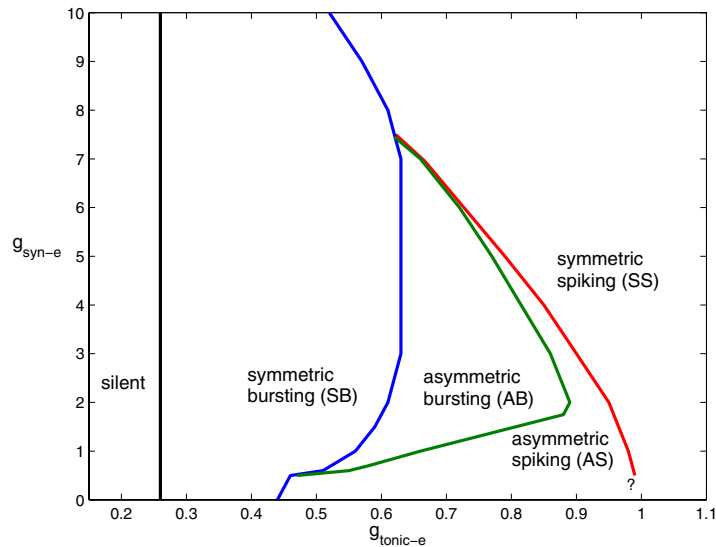


Figure 13. A summary of how the activity of a pair of coupled pre-BötC cells depends on the parameters $g_{tonic-e}, g_{syn-e}$. Each solid curve represents a boundary between regions in $(g_{tonic-e}, g_{syn-e})$ -space corresponding to different activity patterns. The question mark indicates that for very weak coupling g_{syn-e} , numerical difficulties prevent us from distinguishing precisely where the AS \rightarrow SS transition occurs. See the text for a full discussion of the regions and transitions specified in this figure.

3.4.2. Changes in the transition pathway as g_{syn-e} is increased. In Figure 13, the region between the black line and the green curve where it exists, or the blue curve where the green curve does not exist, gives the set of parameter values for which bursting is predicted. This gives excellent quantitative agreement with the simulation results from [2]. Note from Figure 13 that qualitatively different transitions through activity states occur for g_{syn-e} above or below a threshold of approximately 7.5. Figure 14 shows examples of SB and SS solutions for $g_{syn-e} = 8$.

As g_{syn-e} is increased to larger values, the AB and AS regions in $(g_{tonic-e}, g_{syn-e})$ space shrink, as shown in Figure 13. For all $g_{syn-e} < 7.5$, the AS region persists, although it becomes so narrow that it can hardly be distinguished from AB on the scale used in Figure 13. Note that in fact there cannot be a direct transition from SB to AB to SS. That is, in the AB state, the unstable symmetric fixed point p_0 of (6) lies in \mathcal{O} , and in the SS state, this fixed point is stable. The stabilization occurs through a pitchfork bifurcation as $g_{tonic-e}$ is increased, which requires the existence of the two stable equilibria q_A, q_B in \mathcal{O} for $g_{tonic-e}$ sufficiently close to, but below, the onset of SS. For such $g_{tonic-e}$ values, AS will occur.

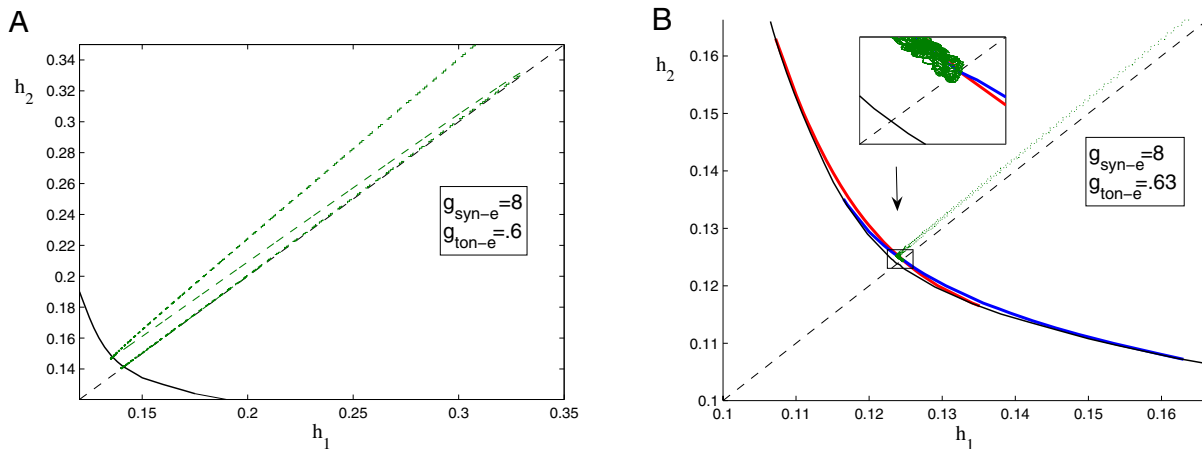


Figure 14. Averaged phase planes from (6), with superimposed trajectories of the full system (1)_i–(4)_i, for $g_{syn-e} = 8$, corresponding to a direct transition from SB to SS. The labels here are as in Figure 11. (A) Symmetric bursting solution for $g_{tonic-e} = .6$. The green trajectory shown travels first from the upper right part of the region to the lower left, where it hits the black boundary curve \mathcal{B} . At this point, the cells enter the silent phase and h_1, h_2 both increase. Correspondingly, the trajectory here moves back from lower left to upper right, although the cells are not spiking and the dynamics of (6) are irrelevant. The jump up to the active phase for the next burst cycle corresponds to the trajectory turning around and heading back toward \mathcal{B} . Note that h_1 and h_2 become closer during the silent phase and jump up, such that the trajectory subsequently travels close to \mathcal{L} (black dashed line). (B) Symmetric spiking solution for $g_{tonic-e} = .63$. The red and blue curves are the nullclines \mathcal{A}_1 and \mathcal{A}_2 , respectively, of (6). The inset shows how the sample trajectory shown approaches the fixed point p_0 where $\mathcal{A}_1 \cap \mathcal{A}_2$ occurs.

In theory, there could be a direct transition from SB to AS, if q_A, q_B were to enter \mathcal{O} before p_0 as $g_{tonic-e}$ were increased. However, our numerical simulations indicate that both the AB and the AS regions terminate together, at $g_{tonic-e} \approx 7.5$. The schematic diagram in Figure 15 illustrates the transition from SB \rightarrow AB \rightarrow AS \rightarrow SS to SB \rightarrow SS that occurs as g_{syn-e} is raised through 7.5. As noted above, Figure 14 gives examples of the dynamics in \mathcal{O}

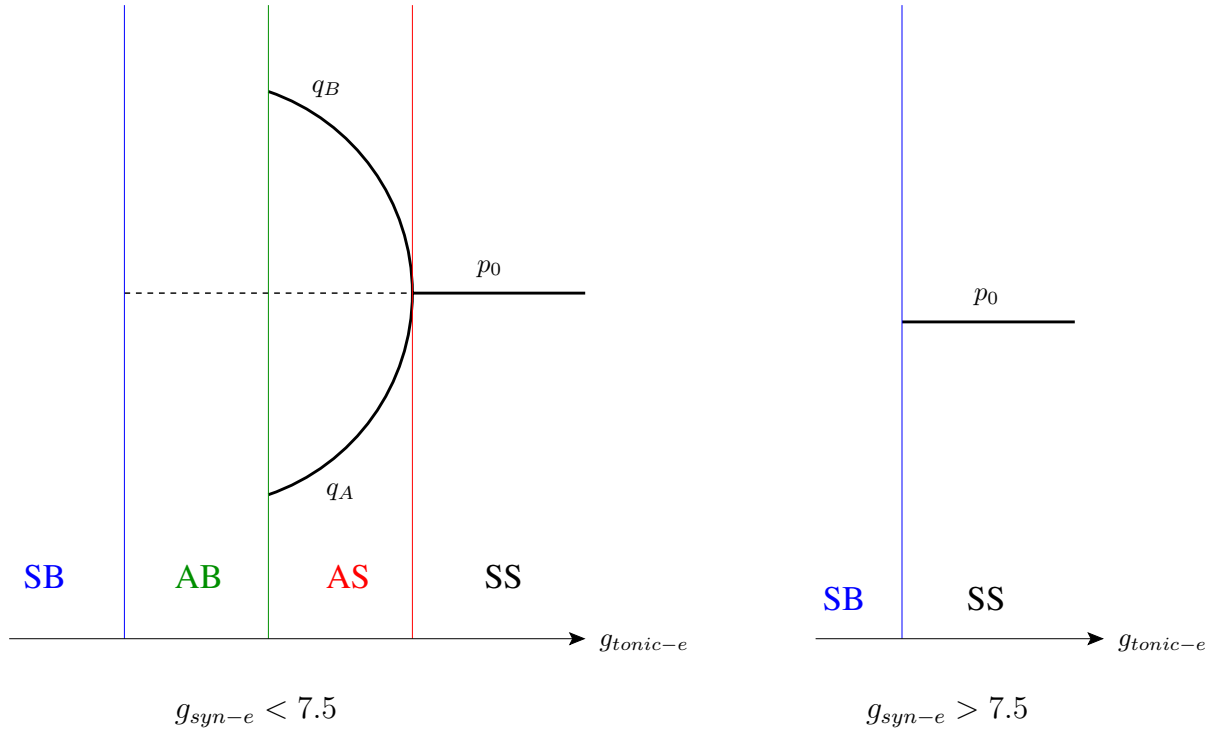


Figure 15. A schematic diagram showing how the change occurs in the bifurcation diagram for the dynamics of (6) inside \mathcal{O} as g_{syn-e} crosses through 7.5. The horizontal black lines indicate the presence of the fixed point p_0 in \mathcal{O} , while the black curves denote the fixed points q_A and q_B ; stable fixed points are given by solid curves, while unstable ones are indicated by dashed curves. As g_{syn-e} increases toward 7.5, the AB and AS regions become narrower, until they cease to exist together at $g_{syn-e} \approx 7.5$.

on both sides of the SB \rightarrow SS transition for $g_{syn-e} = 8$.

3.4.3. Details of activity patterns within regions. The analysis illustrated in Figure 11 characterizes a path in $(g_{tonic-e}, g_{syn-e})$ space along which all four activity states occur as $g_{tonic-e}$ increases. While this same set of transitions arises for an interval of g_{syn-e} values, subtle differences in activity within the same state may emerge for different $(g_{tonic-e}, g_{syn-e})$ values, based on what happens when trajectories leave \mathcal{O} . We next consider a mechanism underlying these differences, and then we briefly return to the issue of synchronization of bursting solutions.

To understand how differences in the details of asymmetric bursting can arise, note that the cells are only coupled through the variables s_i , each of which depends on v_j . For each i , we can consider the (v_i, h_i) bifurcation diagram generated by the dynamics of (v_i, n_i) with h_i as a bifurcation parameter and with s_i also frozen. This will yield a picture similar to those in Figure 2, with the value of s_i (for fixed g_{syn-e}) selecting the relative positions of \mathcal{P} and of the homoclinic orbit that terminates \mathcal{P} ; for s_i treated as a fixed constant in this way, changes in s_i also affect the position of \mathcal{S} , unlike in the right panel of Figure 2. In reality, the s_i have fast dynamics, so one can think of the (v_i, h_i) bifurcation diagram as jumping around rapidly, driven by changes in s_i , but at each instant in time, there exists an appropriate diagram.

Based on this collection of structures, for each fixed $(g_{tonic-e}, g_{syn-e})$, there exists a curve \mathcal{H} of (h, s) -values such that at each value on the curve, the (v, n) -system has a homoclinic orbit. Note that ds/dh is negative on \mathcal{H} (cf. Figure 2); an example appears in Figure 16A. For a trajectory of (6) to exit \mathcal{O} through the boundary curve \mathcal{B} , it is necessary but not sufficient that the (h, s) coordinates for one cell should move to the nonoscillatory side of \mathcal{H} , where no periodic oscillations are supported by the (v_i, n_i) dynamics. If one cell, say, cell 1, does cross \mathcal{H} , then the input from the other cell, via s_1 , may pull it back across, causing regular network oscillations to continue. If this does not happen, then the trajectory of cell 1 will be attracted to the lower branch of \mathcal{S} , causing s_2 to drop. One possibility is that this loss of synaptic input will pull cell 2 across \mathcal{H} as well, terminating the pair's oscillations. This is exactly the case in which exit from \mathcal{O} through variation of one or both of the parameters h_1, h_2 yields an abrupt transition from tonic spiking to quiescence in the fast subsystem $(1)_i, (3)_i, (4)_i$, as illustrated in Figure 16B. For $g_{syn-e} = 3$ and other intermediate values of g_{syn-e} , at least away from a small neighborhood of the AB \rightarrow AS transition, this possibility is realized. Correspondingly, when trajectories of the slow averaged equations (6) that start from initial conditions in \mathcal{O} leave \mathcal{O} , the fast variables stop oscillating altogether and the subsequent silent phase dynamics of the full system $(1)_i-(4)_i$ causes (h_1, h_2) to grow. Eventually, oscillations return, with (h_1, h_2) somewhere in \mathcal{O} , and the dynamics of (6) becomes relevant again.

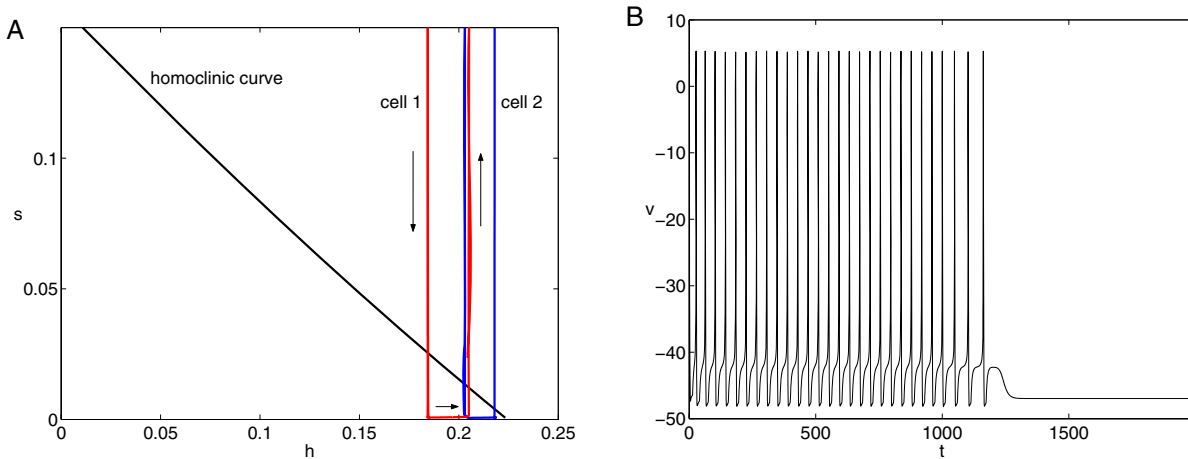


Figure 16. Exit from \mathcal{O} for an asymmetric bursting solution with $g_{syn-e} = 3, g_{tonic-e} = 0.8$. (A) When cell 1 crosses the homoclinic curve (\mathcal{H} in the text) from above to below, it pulls cell 2 down with it, resulting in a cessation of oscillations, with $s_1, s_2 \approx 0$ while h_1, h_2 increase (in the silent phase). The arrows show the direction of time evolution for cell 1, as it transitions from its final oscillation (down arrow) to the silent phase (horizontal arrow) to its return to the active phase (up arrow). The evolution for cell 2 is similar. (B) Correspondingly, the transition across \mathcal{B} yields an abrupt switch from oscillations to quiescence in the dynamics of the fast subsystem $(1)_i, (3)_i$, and $(4)_i$. Here, a crossing of \mathcal{B} was implemented by decreasing h_1 from .169 to .168, at time 999, with $h_2 = .180$. The v time course is only shown for one cell; it was qualitatively similar for the other cell.

An alternative scenario, which arises most prominently for small g_{syn-e} , is that even for $s_2 = 0$, cell 2 can continue to oscillate. In this case, it is possible that successive oscillations of cell 2 can cause cell 1 to resume oscillating after cell 1 crosses \mathcal{H} , even though a single

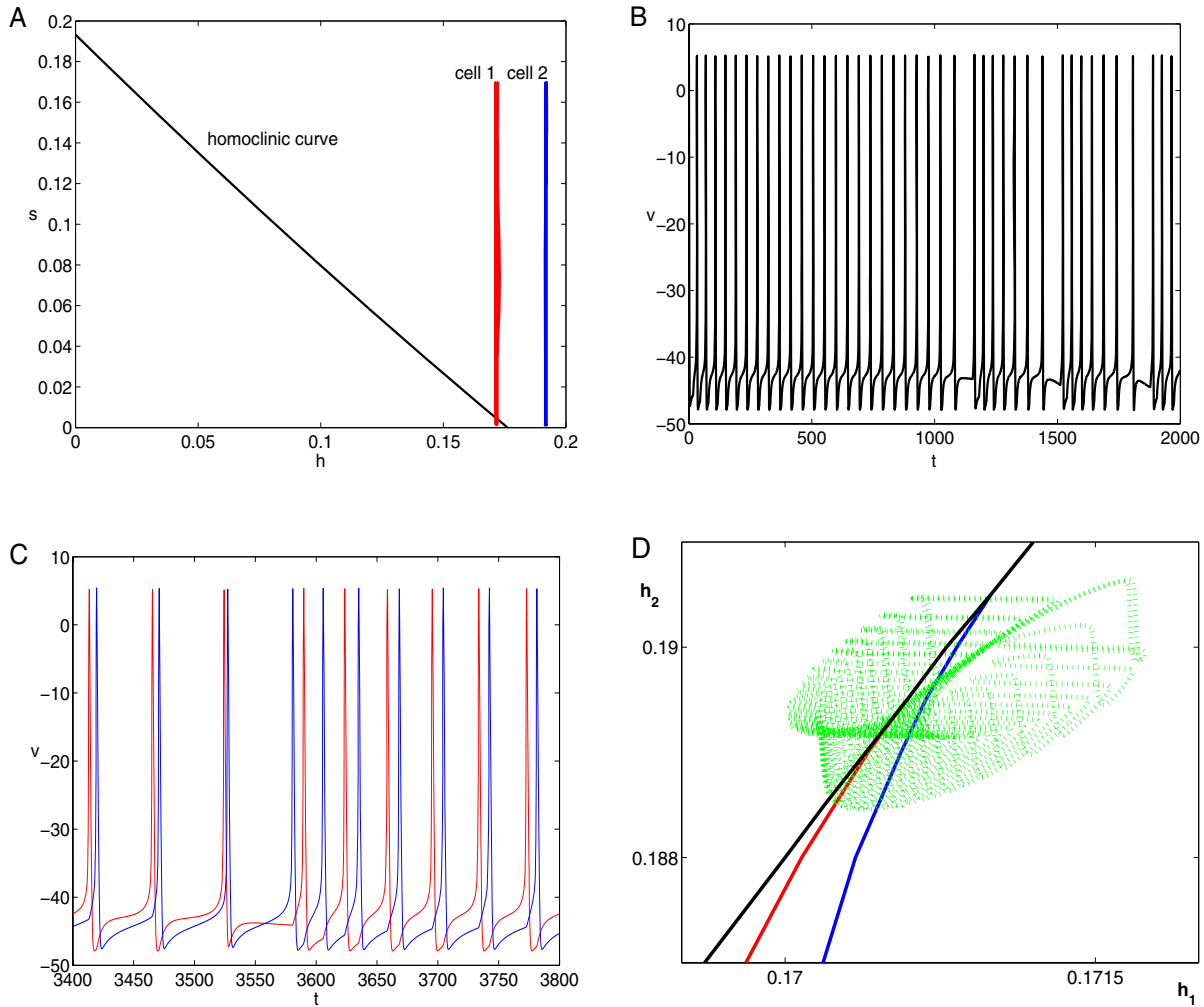


Figure 17. The sustained oscillations of one cell can rescue the oscillations of another cell to which it is coupled, as shown here for $g_{syn-e} = 2, g_{tonic-e} = 0.88$. (A) Even when cell 1 crosses from above to below the curve of homoclinic orbits (\mathcal{H} in the text), cell 2 continues to oscillate. The coupling from cell 2 pulls cell 1 back across \mathcal{H} , where it resumes oscillations. (B) The transition across \mathcal{B} yields a switch from tonic spiking to irregular sustained oscillations in the dynamics of the fast subsystem $(1)_i, (3)_i,$ and $(4)_i$. Here, a crossing of \mathcal{B} was implemented by decreasing h_1 from .1693 to .1692 at time 999, with $h_2 = .205$. The v time course is only shown for one cell; it was qualitatively similar for the other cell. (C) The dynamics of the full system shows asymmetric bursting with short interburst intervals, with a change in burst cycle occurring when cell 2 (blue) fires two consecutive spikes. (D) This asymmetric bursting solution (green) remains very close to \mathcal{B} (black) in the (h_1, h_2) -plane; the red and blue curves show the nullclines $\mathcal{A}_1, \mathcal{A}_2$ of (6) as they terminate on \mathcal{B} .

oscillation of cell 2 does not; in particular, as seen in Figure 17A, cell 2 never crosses \mathcal{H} . When this form of rescued oscillation arises in the fast subsystem $(1)_i, (3)_i, (4)_i$ with h_1, h_2 fixed, as shown in Figure 17B, this does not qualify as regular tonic spiking, and thus by our definition (h_1, h_2) do not lie in \mathcal{O} . Further, this effect yields bursting solutions of the full system $(1)_i-(4)_i$ featuring a very small interburst interval, in which one cell never spends

time in the silent phase; see Figure 17C. Figure 17D shows a corresponding example of an asymmetric bursting solution with $g_{syn-e} = 2$, projected onto the (h_1, h_2) -plane, which differs from that shown in Figure 11B for $g_{syn-e} = 3$ in that the projection of the burst trajectory onto (h_1, h_2) stays very close to \mathcal{B} for all time. If the net drift in (h_1, h_2) during such a solution were actually zero, then there could exist a bursting solution of the full system (1)_i–(4)_i that never enters \mathcal{O} . In summary, the transition across \mathcal{B} corresponds to different fast subsystem dynamics for different $(g_{tonic-e}, g_{syn-e})$ values, leading to differences in the details of the asymmetric bursting that results. We emphasize that the existence of such possibilities does not affect the validity of our analysis of transitions between bursting and tonic spiking; as long as there is no stable fixed point of (6) in \mathcal{O} , regular tonic spiking of the full system will not occur.

Finally, from the idea of considering changes in bifurcation structure as both s and h vary, it becomes clear that the synchronization of the cells in bursting solutions relates in part to a form of fast threshold modulation (FTM) [29, 33]. In theory, FTM can act at either or both of the jump down to the silent phase and the jump up to the active phase. Based on our simulations, most of the compression toward synchrony occurs in the silent phase and in the jump up to the active phase of each burst (e.g., bottom panel of Figure 7). When one cell, say, cell 1, reaches the lower knee of its corresponding critical point curve \mathcal{S}_1 and begins to oscillate, the coupling from cell 1 to cell 2 shifts \mathcal{S}_2 to the left, advancing the jump-up time of cell 2. This can allow compression in the h -coordinates of the cells relative to the uncoupled case, in which h_2 would have had to evolve to larger values before jumping up. During this additional evolution in the uncoupled case, h_1 would have been decreasing, leading to an approximately constant magnitude of $|h_2 - h_1|$ before and after jump-up.

There is also compression in the silent phase, which in theory could be analyzed using the slow dynamics [32, 21]. In the AB case, after this compression and FTM bring trajectories toward synchrony, they are pushed away from the axis of symmetry \mathcal{L} in the active phase by the flow of (6) in \mathcal{O} . In the SB case, no such instability occurs to counteract synchronization. It remains to explore the full details of synchronization of bursts in the SB region in the full 8-dimensional system (1)_i–(4)_i.

4. Burst duration and interburst interval of coupled pre-BötC cells. Our analysis in the previous section explained the dynamic range of bursting of coupled pre-BötC cells. We next give an explanation for the numerically observed changes in burst duration (active phase) and interburst interval (silent phase) under variations of $(g_{syn-e}, g_{tonic-e})$, as shown in Figure 18. The features of the different bursting regimes, symmetric (SB) and asymmetric (AB), are critical for understanding how the burst duration is determined.

4.1. The symmetric bursting regime. The onset of bursting is described in section 3.1 and is due to the crossing of the h -nullsurface \mathcal{G} from the stable lower branch to the unstable middle branch of \mathcal{S} . Recall that this crossing is almost independent of g_{syn-e} , because the position of the lower knee of \mathcal{S} depends only very weakly on g_{syn-e} , and happens at $g_{tonic-e} \approx 0.26$. After the onset of bursting, we are in the symmetric (or top hat) bursting regime, which was analyzed in section 3.3.

If we fix $g_{tonic-e}$ in this SB regime and increase g_{syn-e} , then the burst duration as well as the interburst interval increase. The reason is the following: as g_{syn-e} increases, the Hopf

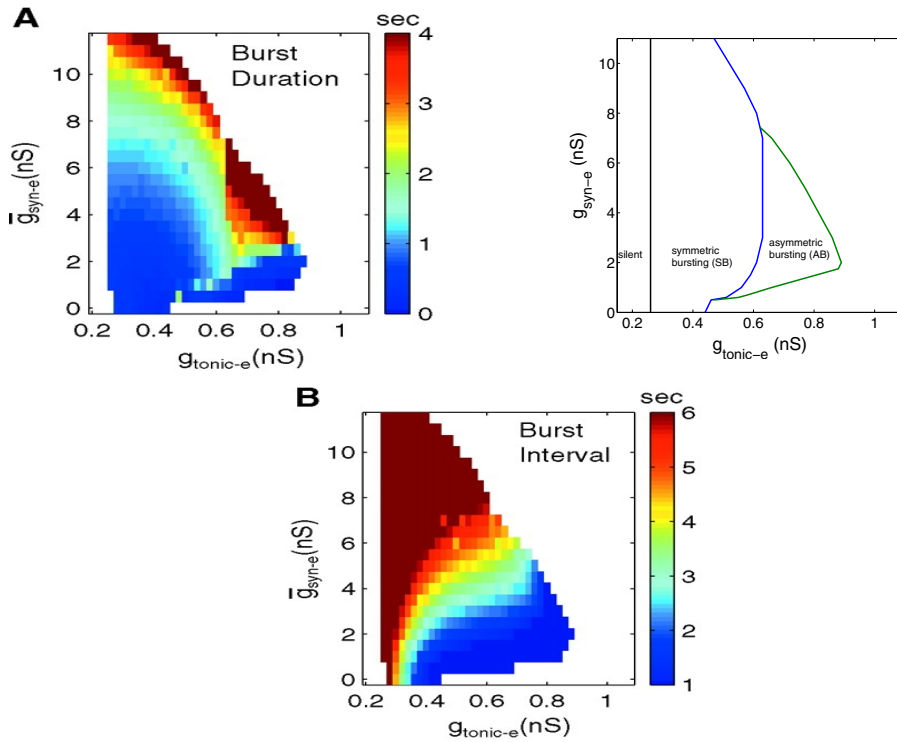


Figure 18. Simulated burst durations and (inter)burst intervals from Butera, Rinzel, and Smith [2]. (A) The color-coded plot shows how burst duration in a pair of coupled pre-BötC cells changes with $g_{tonic-e}$ and g_{syn-e} . The transition curves that we have computed for the onset and offset of symmetric and asymmetric bursting, from Figure 13, are shown for comparison, illustrating in particular that the transition from symmetric to asymmetric bursting is responsible for the abrupt increase in burst duration with $g_{tonic-e}$. (B) Interburst interval increases with g_{syn-e} and decreases as $g_{tonic-e}$ increases. The color-coded plots of burst duration and interburst interval shown here appeared in [2] and are used with permission of the American Physiological Society.

point as well as the stable branch of periodic orbits \mathcal{AP}_S corresponding to the top hat burster move to the left, while the lower knee of \mathcal{S} is fixed, increasing the bistable region of the top hat burster; an example appears in Figure 19A. Thus, solutions stay longer in both the active phase and the silent phase for increased g_{syn-e} .

If we fix g_{syn-e} in the SB regime and increase $g_{tonic-e}$, then the lower knee of \mathcal{S} moves to the left. The Hopf point and the stable branch of periodic orbits \mathcal{AP}_S associated to the top hat burster move to the left as well, but they do so more slowly, as seen in Figure 19B and analogously to what is shown in the bottom left panel of Figure 2. This causes a net decrease in the size of the bistable region. Further, this smaller bistable region is moved to the left, with \mathcal{AP}_S becoming closer to the h -nullsurface \mathcal{G} and the lower branch of \mathcal{S} becoming farther from \mathcal{G} (see, e.g., the bottom row of Figure 3). These changes cause both a slower drift in the active phase and a faster drift in the silent phase. It follows immediately that for increased $g_{tonic-e}$ the interburst interval decreases, because the bistable region gets smaller and the drift

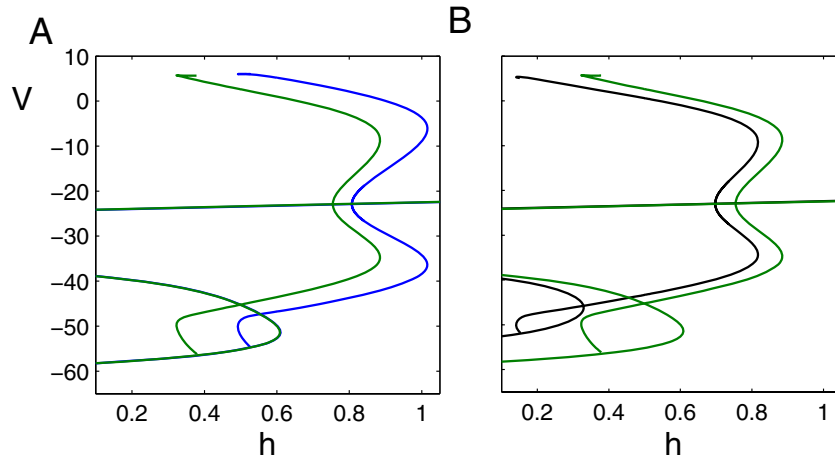


Figure 19. Changes in AP_S induced by changes in g_{syn-e} and $g_{tonic-e}$. (A) With $g_{tonic-e} = 0.3$, increasing g_{syn-e} from 4 (blue) to 8 (green) moves AP_S , and the corresponding Hopf point, to the left, while the lower knee of S remains unchanged. (B) With $g_{syn-e} = 8$, increasing $g_{tonic-e}$ from 0.3 (green) to 0.6 (black) moves both AP_S and the lower knee of S to the left. (Note that the green copies of AP_S in both panels are identical.)

in the silent phase becomes faster.

On the other hand, although the bistable region gets smaller, the slower drift in the active phase counters this effect and in fact causes the burst duration to increase with $g_{tonic-e}$. To understand why the slower drift dominates, recall from section 3.3 that the transition from bursting to spiking in the analysis of the top hat burster is described by a zero drift condition $a(h_L) = 0$ of system (5), which describes the averaged evolution of h during the active phase. For values of $g_{syn-e} > 7.5$, this analysis captures the transition from bursting to spiking of coupled pre-BötC cells. In this parameter regime, the average drift in the active phase decreases to zero with increasing $g_{tonic-e}$, causing the transition to spiking. Since the size of the bistable region is bounded away from 0 because of the folded termination of the top hat structure, this slowing overcomes the shrinking of the bistable region and thus the burst duration generally increases with increasing $g_{tonic-e}$.

For intermediate and lower values $g_{syn-e} \leq 7.5$, the increase of burst duration with increasing $g_{tonic-e}$ still occurs in the SB regime, by the same argument. However, the zero drift condition (for $h_1 = h_2$) now corresponds to the appearance of the unstable fixed point p_0 in \mathcal{O} and thus determines the transition from SB to AB, given by the blue curve in Figure 18, rather than the transition from SB to SS. Changes in burst duration in the AB region are discussed in the following subsections.

4.2. The asymmetric bursting regime for moderate and large $g_{syn-e} \leq 7.5$. Here we discuss the abrupt change in burst duration seen at the transition from SB to AB (Figure 18A), the impact of $g_{tonic-e}$ and g_{syn-e} on burst duration within AB, and the impact of $g_{tonic-e}$ and g_{syn-e} on interburst interval within AB, for $g_{syn-e} \leq 7.5$ but not too small.

The AB regime was analyzed in section 3.4 via the study of the reduced system (6). The appearance of the saddle point p_0 in (h_1, h_2) -space forces solutions to leave the neighborhood of the symmetry axis \mathcal{L} (see Figure 11B). This scenario causes a very sharp increase in burst duration near the onset of asymmetric bursting. More precisely, AB solutions of system (6)

follow close to \mathcal{L} , heading toward the boundary \mathcal{B} of the oscillatory region \mathcal{O} . Once they pass close to the saddle point p_0 , however, they are diverted to a path between the nullclines $\mathcal{A}_1, \mathcal{A}_2$ and the curve \mathcal{B} , crossing both \mathcal{A}_1 and \mathcal{A}_2 before they can reach \mathcal{B} and jump from the active phase to the silent phase (see Figure 11B). This excursion can be of quite substantial duration even for $g_{tonic-e}$ close to the SB \rightarrow AB transition, depending on where $\mathcal{A}_1, \mathcal{A}_2$ lie relative to \mathcal{B} . Thus, this phase plane analysis for the reduced system (6) explains nicely the sharp increase in burst duration seen in Figure 18A. Note in particular that the “discontinuity” observed in the burst duration as $g_{tonic-e}$ is increased matches exactly the SB \rightarrow AB transition curve for $7.5 \geq g_{syn-e} \geq 3$.

The transition from AB to AS happens due to the appearance of two asymmetric stable fixed points, q_A and q_B , in the phase space of system (6), as shown in Figure 11C. These fixed points correspond to two new intersection points of the (convex) nullclines \mathcal{A}_1 and \mathcal{A}_2 . Thus, with increasing $g_{tonic-e}$ in the AB regime, \mathcal{A}_1 and \mathcal{A}_2 get closer until they intersect in the oscillatory region \mathcal{O} at the transition value of $g_{tonic-e}$. Therefore, as $g_{tonic-e}$ increases, solutions will spend more time following the path between the nullclines \mathcal{A}_1 and \mathcal{A}_2 and the boundary \mathcal{B} before leaving \mathcal{O} ; as a result, the burst duration increases with increasing $g_{tonic-e}$.

The same argument holds also for fixed $g_{tonic-e}$ and increasing g_{syn-e} ; that is, the burst duration will increase due to the geometry of the nullclines. With increasing g_{syn-e} , \mathcal{A}_1 and \mathcal{A}_2 again get closer, and pull away from \mathcal{B} , before they intersect at the transition to AS. Therefore, the burst duration increases monotonically with increasing g_{syn-e} .

The interburst interval behaves the same as in the symmetric case, because the bistable region of each of the oscillators increases with increasing g_{syn-e} , with no change in position relative to \mathcal{G} in the silent phase, and decreases with increasing $g_{tonic-e}$, with an increased distance from \mathcal{G} in the silent phase. Correspondingly, the interburst interval increases with increasing g_{syn-e} and decreases with increasing $g_{tonic-e}$ as well.

Finally, the smaller bistable region that occurs for larger $g_{tonic-e}$ can mitigate the increases in burst duration, discussed above, somewhat, but as in the previous subsection, the bistable region size is bounded away from zero by the top hat structure, and a net increase in burst duration occurs as $g_{tonic-e}$ is increased. We shall see in subsection 4.3 that this relation may differ for smaller g_{syn-e} .

4.3. Asymmetric bursting for small g_{syn-e} . As seen in Figure 20, the top hat structure of \mathcal{AP}_S can be eliminated either by decreasing g_{syn-e} for fixed $g_{tonic-e}$ or by increasing $g_{tonic-e}$ for fixed g_{syn-e} , yielding a transition from top hat bursting back to square-wave bursting. This transition happens at smaller $g_{tonic-e}$ for smaller g_{syn-e} (e.g., near $g_{tonic-e} = 0.6$ for $g_{syn-e} = 2$ and near $g_{tonic-e} = 0.4$ for $g_{syn-e} = 0.1$).

Within both the top hat and the square-wave scenarios, it is possible for the fast subsystem to feature bistability between periodic orbits on \mathcal{AP}_S and critical points on the lower branch of \mathcal{S} . In the top hat case, this bistability is always present. As a result of the transition back to the square-wave scenario, however, it is possible for the size of the bistable region for the fast subsystem to go to zero, corresponding to a saddle-node on an invariant circle, or SNIC, bifurcation in which the homoclinic point that terminates \mathcal{AP} lies on the lower knee of \mathcal{S} , as $g_{tonic-e}$ increases. Thus, the outcome of the competition between slower drift in the active phase and shrinkage of the bistable region as $g_{tonic-e}$ increases, and correspondingly

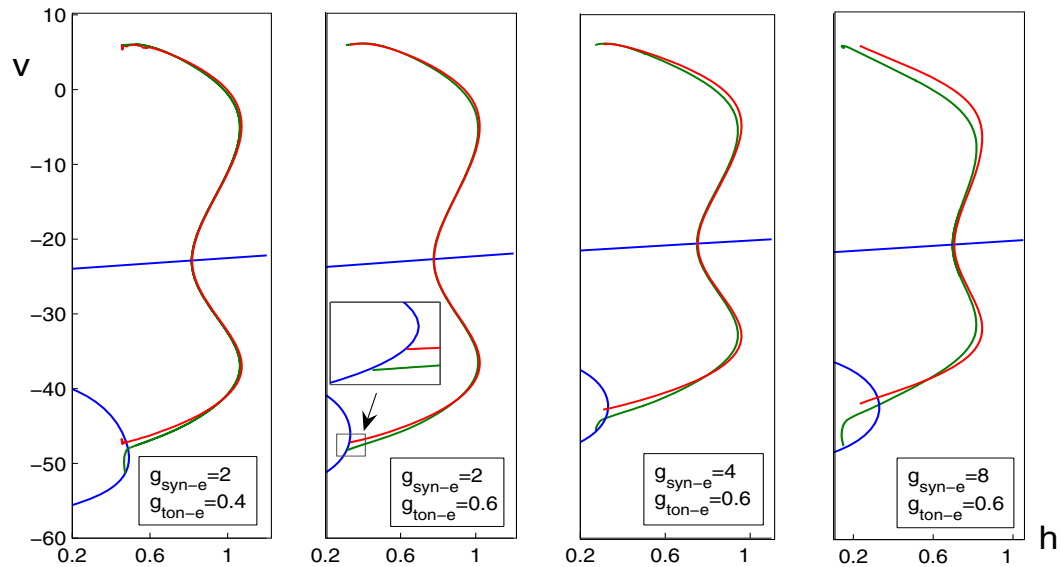


Figure 20. Changes in the antiphase (green) and in-phase (red) periodic orbit families as $g_{tonic-e}$ and g_{syn-e} vary. As $g_{tonic-e}$ is increased for fixed g_{syn-e} , the antiphase family switches from three branches, connected by two saddle-node bifurcations, to two branches, corresponding to the switch from top hat bursting to square-wave bursting. Lowering g_{syn-e} for fixed $g_{tonic-e}$ has a similar effect.

the changes in burst duration with $g_{tonic-e}$, cannot be predicted. On the other hand, the shrinking bistable region and accelerating flow in the silent phase still synergistically induce shorter interburst intervals for larger $g_{tonic-e}$, as discussed previously for larger g_{syn-e} .

5. Discussion. This work represents an effort to explain the finding that the introduction of synaptic coupling in a network of model pre-BötC cells, relevant to respiratory rhythms, extends the range of parameters over which synchronized bursting oscillations occur, relative to the uncoupled case. Many subtle issues lurk within this finding, including differences in the effects of within-network coupling (I_{syn-e} in (1)) versus external tonic coupling ($I_{tonic-e}$ in (1)) and a wide range of complex changes in burst characteristics with changes in the strengths of these inputs. Using geometric fast/slow analysis of a two-cell network, we find that the introduction of synaptic coupling qualitatively changes the class of bursting seen in the network, from square-wave bursting to *top hat bursting* or fold/fold cycle bursting [11], except possibly for a small range of parameters with small coupling strengths. Further, through a progression of levels of analysis, we have shown that the apparent transition from bursting to tonic spiking can actually encompass a transition from symmetric bursting to asymmetric bursting to asymmetric spiking to symmetric spiking, with significant implications for burst characteristics that we analyze using the two-variable slow averaged system (6). In particular, the fact that the cells' spikes are out of phase in the solutions observed plays a key role in extending the dynamic range of bursting to larger $g_{tonic-e}$.

While the equations that we have studied were introduced to model particular cells impli-

cated in the generation of respiratory rhythms, dynamically they give rise to generic square-wave bursting, and hence the qualitative aspects of our results apply directly to general pairs of coupled square-wave bursters. Past work has shown that the introduction of diffusive coupling between two square-wave bursters can split the associated family of periodic solutions into an unstable in-phase family and an antiphase family, with an associated increase in burst period [25, 5]. This finding is similar to what we report here with synaptic coupling, although in the diffusive case the antiphase family is stable and affects period only when coupling is weak, whereas we find that it remains stable for strong synaptic coupling. Further, in addition to demonstrating that this splitting occurs, we note that qualitative changes in burst pattern result from the saddle-node termination of the stable antiphase periodic branch, as also noted in [11, 27, 4, 26]. An additional difference between the diffusive and synaptic analyses is that the analysis done for diffusive coupling capitalizes on the observation that $h_2 - h_1 \approx \text{constant}$, where h_i is the slow variable for cell i , to focus on the single bifurcation parameter $\delta = (h_2 - h_1)/2$ for the coupled system. In the synaptic case, we have shown that this single slow variable picture fails to capture the full dynamic range of bursting, which we have explained using analysis of a two-variable slow averaged system. This approach allows us to consider a range of dynamic effects resulting from turning on and varying the strength of synaptic coupling, including complex changes in burst duration and interburst interval, in addition to transitions between asymmetric and symmetric bursting and tonic spiking states.

Clearly, it will be interesting to see whether the effects of changes in g_{syn-e} and $g_{tonic-e}$ on pre-BötC activity patterns predicted by this analysis can be observed experimentally. In an experimental recording, if different cells' voltage and persistent sodium current time courses were identical, except for a systematic time shift, then the network activity pattern could be classified as symmetric, whereas other differences in these time courses across different (coupled) cells would characterize asymmetric activity patterns. Our results indicate that asymmetric states would be present only if g_{syn-e} were not too large. Of course, noise would complicate the distinction between symmetry and asymmetry. Interestingly, the analysis in subsection 4.3 points out that bistability of periodic and rest states may be lost as $g_{tonic-e}$ increases for relatively small g_{syn-e} . This leads to the prediction, illustrated in Figure 21, that transient, hyperpolarizing inputs to tonic spiking solutions could be used to gauge the strength of synaptic coupling in an experimental preparation. More precisely, for large enough g_{syn-e} , such an input would lead to a prolonged delay before return to spiking, because it would induce a prolonged excursion along a branch of stable steady states of the fast subsystem, as seen in Figure 21 A,B. On the other hand, for sufficiently small g_{syn-e} , bistability would be lost, and the effects of a transient, hyperpolarizing input would be gone as soon as the input were terminated, as seen in Figure 21 C,D.

We use a fast/slow decomposition in the singular limit, in which solutions consist of trajectories generated by a slow subsystem, connected by jumps formed by solutions of a fast subsystem. This approach has been used effectively in past analyses of bursting (e.g., [19, 20, 22]), and rigorous analysis has shown that sufficiently close to the singular limit, for most initial conditions, trajectories of square-wave bursters behave similarly to such concatenated solutions [31, 30, 16]. In the case of the pre-BötC in particular, the predictions from our fast/slow analysis yield good quantitative agreement with past simulation results [2] while explaining the mechanisms underlying many of the burst characteristics that were observed

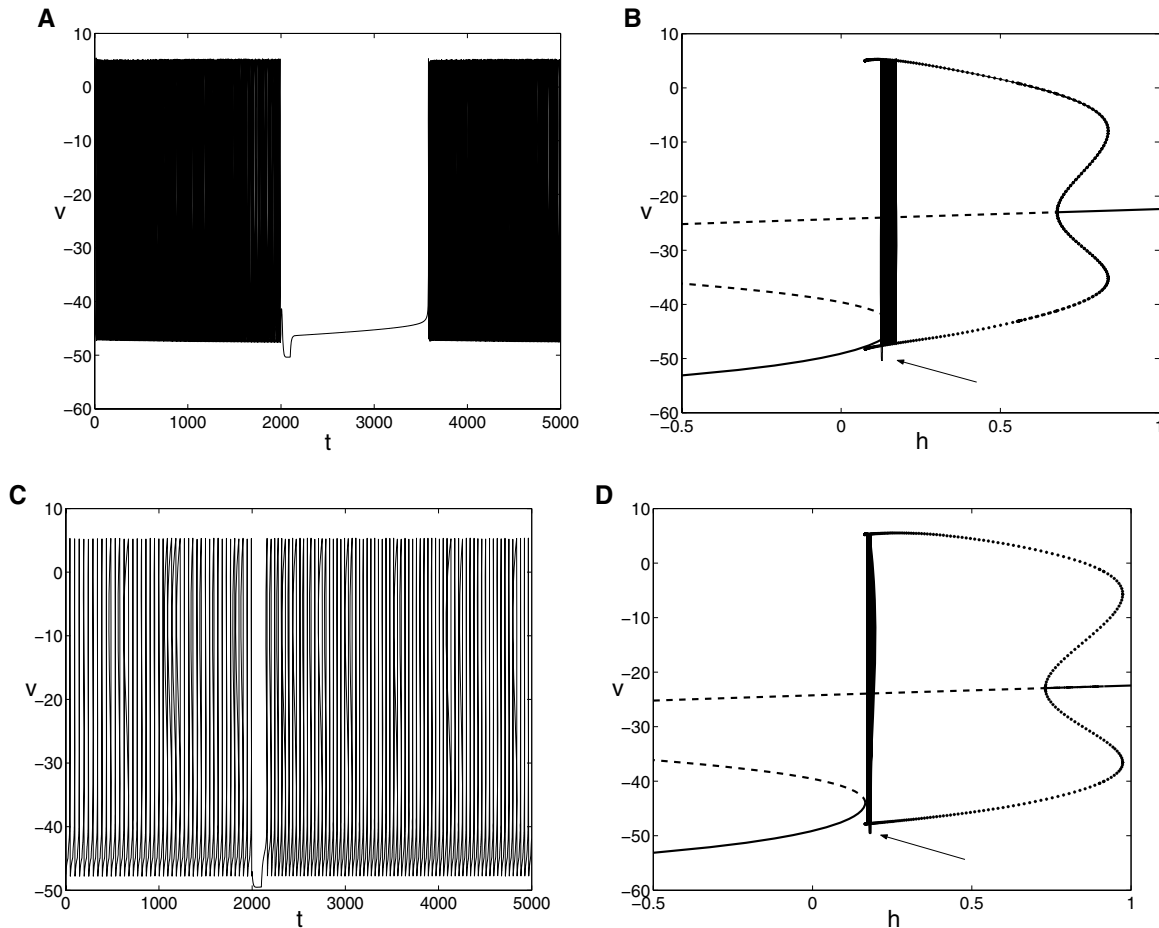


Figure 21. Effects of transient, hyperpolarizing inputs on tonic spiking solutions. (A) With $(g_{tonic-e}, g_{syn-e}) = (0.9, 5)$, a hyperpolarizing input of 100 msec leads to a prolonged delay before tonic spiking resumes. (B) Bifurcation diagram showing a critical point curve (solid stable points and dashed unstable points) and the family of antiphase periodic orbits \mathcal{AP} (thick dotted curve) for the fast subsystem for $(g_{tonic-e}, g_{syn-e}) = (0.9, 5)$. The (h, v) coordinates of the trajectory from (A) are superimposed. Before the input, this trajectory consists of an oscillation with h at a constant value below the knee of the critical point curve. The initial effect of hyperpolarization is to pull the trajectory below \mathcal{AP} , as marked by the arrow. After this, the trajectory makes a prolonged excursion along the branch of stable critical points before jumping toward \mathcal{AP} and then drifting leftward, back to the h -value where it started. (C) With $(g_{tonic-e}, g_{syn-e}) = (0.9, 1)$, cessation of a 100 msec hyperpolarizing input leads to an immediate return to tonic spiking. (D) Bifurcation diagram and trajectory for $(g_{tonic-e}, g_{syn-e}) = (0.9, 1)$, labeled as in (B). The arrow shows the small drop in v due to hyperpolarization.

in the simulations. However, the rigorous extension of these ideas beyond the singular limit remains to be performed.

Clearly, our study of a pair of synaptically coupled cells has yielded new insights into the fundamental influences of $g_{tonic-e}$ and g_{syn-e} and the role of asynchrony of spikes. To understand fully the bursting dynamics observed in the pre-BötC experimentally, additional biological features will need to be considered, starting with the addition of more cells and the

inclusion of heterogeneity in parameter values and features across cells. Indeed, heterogeneity in parameters was observed to enhance the robustness of synchronized bursting in simulations, and while we have analyzed conditions for synchrony in the presence of heterogeneity previously [23], that work focused on a reduced model and on a restricted class of heterogeneities. Further, it appears that there may be heterogeneous ionic mechanisms that contribute to rhythmic oscillations across an entire pre-BötC cell network [6, 17, 7], and the interactions of multiple mechanisms could be a rich source of network dynamics. Finally, while this work has focused on synchronized bursting, experiments have shown that modifications, such as increases in external potassium concentration or decreases in g_{syn-e} , can lead to clustered or aperiodic behavior [8, 24]. Since various quasiperiodic and mixed-mode oscillations have been observed in spontaneous breathing of human infants and neonatal rodents [8], it will be important to analyze transitions away from full-population bursting to characterize fully the dynamics of the pre-BötC.

Appendix. Equations (1), (2), and (3) were introduced in [1], while the synaptic equation (4) is given in [2]. In these equations, for $x \in \{m_P, m, h, n, s\}$, the function $x_\infty(v)$ takes the form $x_\infty(v) = \{1 + \exp[(v - \theta_x)/\sigma_x]\}^{-1}$, and for $x \in \{h, n\}$, the function $\tau_x(v)$ takes the form $\tau_x(v) = \bar{\tau}_x / \cosh[(v - \theta_x)/2\sigma_x]$. The parameter values used in these equations are listed in the table below.

Parameter	Value	Parameter	Value	Parameter	Value	Parameter	Value
g_{NaP}	2.8 nS	E_{Na}	50.0 mV	$\theta_{m,P}$	-40 mV	$\sigma_{m,P}$	-6 mV
		$\bar{\tau}_h/\epsilon$	10000 msec	θ_h	-48 mV	σ_h	6 mV
g_{Na}	28 nS			θ_m	-34 mV	σ_m	-5 mV
g_K	11.2 nS	E_K	-85.0 mV				
		$\bar{\tau}_n$	10 msec	θ_n	-29 mV	σ_n	-4 mV
g_L	2.8 nS	E_L	-65.0 mV	C	21 pF	E_{syn-e}	0 mV
α_s	0.2 msec ⁻¹	τ_s	5 msec	θ_s	-10.0 mV	σ_s	-5 mV

Acknowledgments. We thank Jeff Smith for encouraging us to think about the dynamic range of bursting in the pre-BötC and Rob Butera for providing the simulation data from [2] shown in Figure 18.

REFERENCES

- [1] R.J. BUTERA, J. RINZEL, AND J.C. SMITH, *Models of respiratory rhythm generation in the pre-Bötzinger complex. I. Bursting pacemaker neurons*, J. Neurophysiol., 82 (1999), pp. 382–397.
- [2] R.J. BUTERA, J. RINZEL, AND J.C. SMITH, *Models of respiratory rhythm generation in the pre-Bötzinger complex. II. Populations of coupled pacemaker neurons*, J. Neurophysiol., 82 (1999), pp. 398–415.
- [3] T.R. CHAY AND J. RINZEL, *Bursting, beating, and chaos in an excitable membrane model*, Biophys. J., 47 (1985), pp. 357–366.
- [4] G. CYMBALYUK AND A. SHILNIKOV, *Coexistence of tonic spiking oscillations in a leech neuron model*, J. Comp. Neurosci., 18 (2005), pp. 255–263.
- [5] G. DE VRIES AND A. SHERMAN, *Beyond synchronization: Modulatory and emergent effects of coupling in square-wave bursting*, in BURSTING: The Genesis of Rhythm in the Nervous System, S. Coombes and P. C. Bressloff, eds., World Scientific, River Edge, NJ, 2005, pp. 243–272.
- [6] C.A. DEL NEGRO, C. MORGADO-VALLE, AND J.L. FELDMAN, *Respiratory rhythm: An emergent network property?*, Neuron, 34 (2002), pp. 821–830.

- [7] C.A. DEL NEGRO, C. MORGADO-VALLE, J.A. HAYES, D.D. MACKAY, R.W. PACE, E.A. CROWDER, AND J.L. FELDMAN, *Sodium and calcium current-mediated pacemaker neurons and respiratory rhythm generation*, *J. Neurosci.*, 25 (2005), pp. 446–453.
- [8] C.A. DEL NEGRO, C.G. WILSON, R.J. BUTERA, H. RIGATTO, AND J.C. SMITH, *Periodicity, mixed-mode oscillations, and quasiperiodicity in a rhythm-generating neural network*, *Biophys. J.*, 82 (2002), pp. 206–214.
- [9] B. ERMENTROUT, *Simulating, Analyzing, and Animating Dynamical Systems: A Guide to XPPAUT for Researchers and Students*, Software Environ. Tools 14, SIAM, Philadelphia, 2002.
- [10] G.B. ERMENTROUT AND N. KOPELL, *Multiple pulse interactions and averaging in systems of coupled neural oscillators*, *J. Math. Biol.*, 29 (1991), pp. 195–217.
- [11] E. IZHIKEVICH, *Neural excitability, spiking, and bursting*, *Internat. J. Bifur. Chaos Appl. Sci. Engrg.*, 10 (2000), pp. 1171–1266.
- [12] S.M. JOHNSON, J.C. SMITH, G.D. FUNK, AND J.L. FELDMAN, *Pacemaker behavior of respiratory neurons in medullary slices from neonatal rat*, *J. Neurophysiol.*, 72 (1994), pp. 2598–2608.
- [13] N. KOPELL, *Toward a theory of modelling central pattern generators*, in *The Neural Control of Rhythmic Movements in Vertebrates*, A. Cohen, H. Rossignol, and S. Grillner, eds., Wiley, New York, 1988, pp. 369–413.
- [14] N. KOSHIYA AND J.C. SMITH, *Neuronal pacemaker for breathing visualized in vitro*, *Nature*, 400 (1999), pp. 360–363.
- [15] Y.A. KUZNETSOV, *Elements of Applied Bifurcation Theory*, 2nd ed., Springer-Verlag, New York, 1998.
- [16] E. LEE AND D. TERMAN, *Uniqueness and stability of periodic bursting solutions*, *J. Differential Equations*, 158 (1999), pp. 48–78.
- [17] F. PEÑA, M.A. PARKIS, A.K. TRYBA, AND J.-M. RAMIREZ, *Differential contribution of pacemaker properties to the generation of respiratory rhythms during normoxia and hypoxia*, *Neuron*, 43 (2004), pp. 105–117.
- [18] J.-M. RAMIREZ, U.J.A. QUELLMALZ, AND D.W. RICHTER, *Postnatal changes in the mammalian respiratory network as revealed by the transverse brain stem slice of mouse*, *J. Physiol. (Lond.)*, 491 (1996), pp. 799–812.
- [19] J. RINZEL, *Bursting oscillations in an excitable membrane model*, in *Ordinary and Partial Differential Equations*, B.D. Sleeman and R.J. Jarvis, eds., Springer-Verlag, Berlin, 1985, pp. 304–316.
- [20] J. RINZEL, *A formal classification of bursting mechanisms in excitable systems*, in *Proceedings of the International Congress of Mathematics*, A.M. Gleason, ed., AMS, Providence, RI, 1987, pp. 1578–1593.
- [21] J. RUBIN AND D. TERMAN, *Geometric analysis of population rhythms in synaptically coupled neuronal networks*, *Neural Comput.*, 12 (2000), pp. 597–645.
- [22] J. RUBIN AND D. TERMAN, *Geometric singular perturbation analysis of neuronal dynamics*, in *Handbook of Dynamical Systems, Vol. 2: Towards Applications*, B. Fiedler, ed., North-Holland, Amsterdam, 2002, pp. 93–146.
- [23] J. RUBIN AND D. TERMAN, *Synchronized activity and loss of synchrony among heterogeneous conditional oscillators*, *SIAM J. Appl. Dyn. Syst.*, 1 (2002), pp. 146–174.
- [24] I.A. RYBAK, N.A. SHEVTSOVA, W.M. ST-JOHN, J.F.R. PATON, AND O. PIERREFICHE, *Endogenous rhythm generation in the pre-Bötzinger complex and ionic currents: Modelling and in vitro studies*, *European J. Neurosci.*, 18 (2003), pp. 239–257.
- [25] A. SHERMAN, *Antiphase, asymmetric, and aperiodic oscillations in excitable cells. I. Coupled bursters*, *Bull. Math. Biol.*, 56 (1994), pp. 811–835.
- [26] A. SHILNIKOV, R. CALABRESE, AND G. CYMBALYUK, *Mechanism of bistability: Tonic spiking and bursting in a neuron model*, *Phys. Rev. E*, 71 (2005), 056214.
- [27] A. SHILNIKOV AND G. CYMBALYUK, *Homoclinic bifurcations of periodic orbits en a route from tonic spiking to bursting in neuron models*, *Reg. Chaotic Dyn.*, 9 (2004), pp. 281–297.
- [28] J.C. SMITH, H.H. ELLENBERGER, K. BALLANYI, D.W. RICHTER, AND J.L. FELDMAN, *Pre-Bötzinger complex: A brainstem region that may generate respiratory rhythm in mammals*, *Science*, 254 (1991), pp. 726–729.
- [29] D. SOMERS AND N. KOPELL, *Rapid synchronization through fast threshold modulation*, *Biol. Cybernet.*, 68 (1993), pp. 393–407.

-
- [30] D. TERMAN, *Chaotic spikes arising from a model of bursting in excitable membranes*, SIAM J. Appl. Math., 51 (1991), pp. 1418–1450.
 - [31] D. TERMAN, *The transition from bursting to continuous spiking in an excitable membrane model*, J. Nonlinear Sci., 2 (1992), pp. 133–182.
 - [32] D. TERMAN, N. KOPELL, AND A. BOSE, *Dynamics of two mutually coupled inhibitory neurons*, Phys. D, 117 (1998), pp. 241–275.
 - [33] D. TERMAN AND D. L. WANG, *Global competition and local cooperation in a network of neural oscillators*, Phys. D, 81 (1995), pp. 148–176.